Volume 18
Number 3
7 February 2025
Pages 1041–1574

Energy & Environmental Science

rsc.li/ees

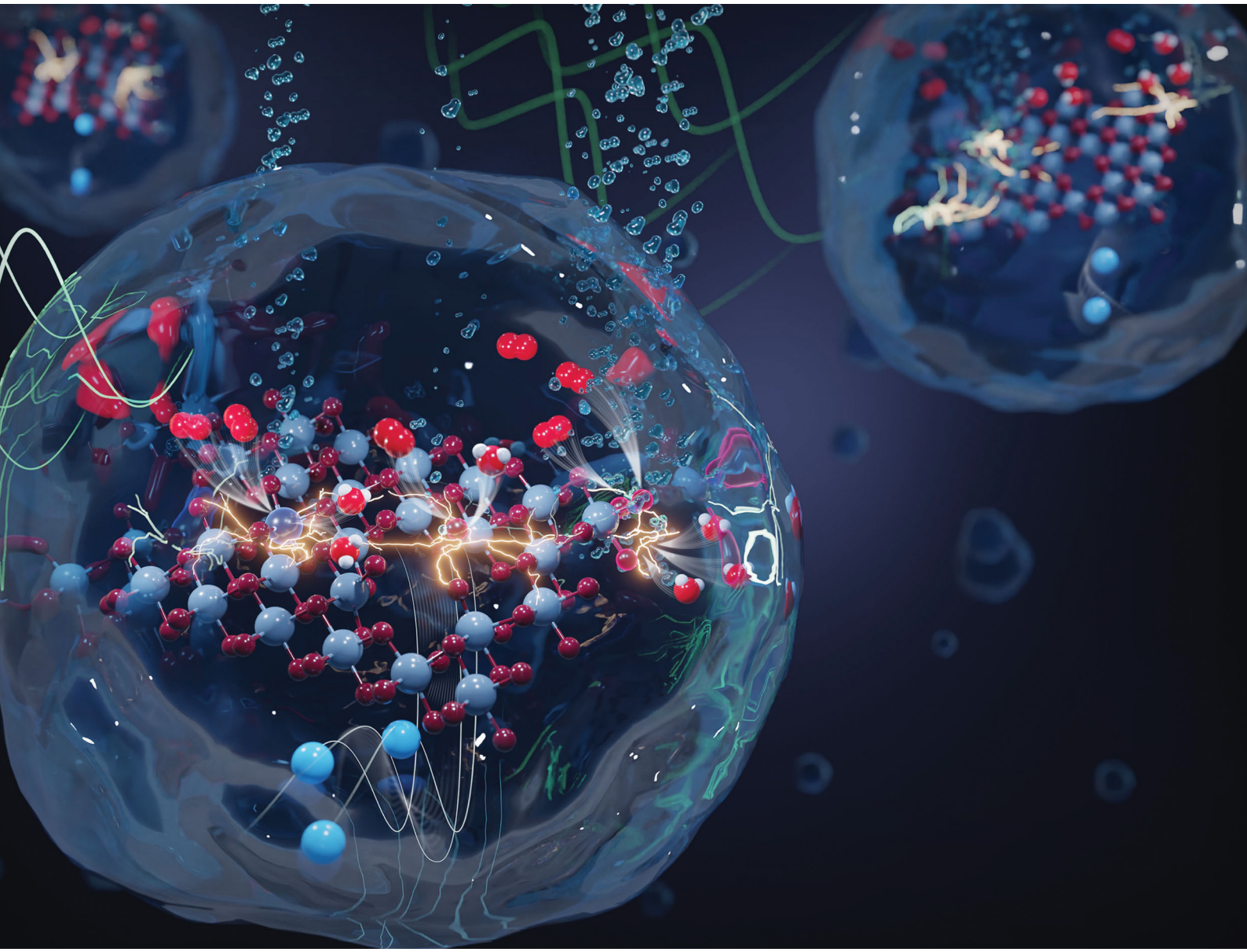

ISSN 1754-5706

ROYAL SOCIETY OF CHEMISTRY

PAPER

Marianne van der Merwe, Yonghyuk Lee, Raul Garcia-Diez *et al.*
Unravelling the mechanistic complexity of the oxygen evolution reaction and Ir dissolution in highly dimensional amorphous hydrous iridium oxides

Energy & Environmental Science

ROYAL SOCIETY OF CHEMISTRY

PAPER

View Article Online
View Journal | View Issue

Cite this: *Energy Environ. Sci.*, 2025, **18**, 1214

Unravelling the mechanistic complexity of the oxygen evolution reaction and Ir dissolution in highly dimensional amorphous hydrous iridium oxides†

Marianne van der Merwe, *[a] Yonghyuk Lee, *[b] Romualdus Enggar Wibowo, [a] Tathiana Kokumai, [a] Anna Efimenko,[ac] Mauricio D. Arce, [ad] Catalina E. Jimenez, [a] Benjamin Howchen, [a] Rosario Suarez Anzorena, [ae] Ilaria Lucentini,[f] Carlos Escudero, [f] Götz Schuck, [g] Zdravko Kochovski, [h] Marco Favaro, [i] David E. Starr, [i] Karsten Reuter, [b] Christoph Scheurer, [bj] Marcus Bär [ackl] and Raul Garcia-Diez *[a]

Understanding the oxygen evolution reaction (OER) and Ir dissolution mechanisms in amorphous, hydrous iridium oxides (am-hydr-IrO_x) is hindered by the reliance on crystalline iridium oxide theoretical models to interpret its behaviour. This study presents a comprehensive investigation of hydrous iridium oxide thin films (HIROFs) as a model for am-hydr-IrO_x to elucidate electronic and structural transformations under OER conditions of proton exchange membrane water electrolyzers (PEM-WE). Employing *in situ* and *operando* Ir L_3-edge X-ray absorption spectroscopy supported by density functional theory calculations, we introduce a novel surface H-terminated nanosheet model that better characterizes the short-range structure of am-hydr-IrO_x compared to previous crystalline models, which exhibits elongated Ir–O bond lengths compared to rutile-IrO_2. This atomic model unveils the electronic and structural transformations of am-hydr-IrO_x, progressing from H-terminated nanosheets to structures with multiple Ir vacancies and shorter bond-lengths at OER potentials. Notably, Ir dissolution emerges as a spontaneous, thermodynamically driven process, initiated at potentials lower than OER activation, which requires a parallel mechanistic framework describing Ir dissolution by Ir defect formation. Moreover, our results provide mechanistic insights into the activity-stability relationship of am-hydr-IrO_x by systematically screening the DFT-calculated OER activity of diverse Ir and O chemical environments. This work challenges conventional perceptions of iridium dissolution and OER mechanisms in am-hydr-IrO_x, providing an alternative perspective within a dual-mechanistic framework.

Received 28th June 2024,
Accepted 27th November 2024

DOI: 10.1039/d4ee02839b

rsc.li/ees

[a] *Interface Design, Helmholtz Zentrum Berlin für Materialien und Energie GmbH (HZB), Albert-Einstein-Str. 15, 12489 Berlin, Germany. E-mail: marianne.vdm@helmholtz-berlin.de, raul.garcia_diez@helmholtz-berlin.de*
[b] *Fritz-Haber-Institut der Max-Planck-Gesellschaft, Faradayweg 4–6, 14195 Berlin, Germany. E-mail: ylee@fhi-berlin.mpg.de*
[c] *Energy Materials In situ* Laboratory Berlin (EMIL), HZB, Albert-Einstein-Str. 15, 12489 Berlin, Germany
[d] *Departamento Caracterización de Materiales, INN-CNEA-CONICET, Centro Atómico Bariloche, Av. Bustillo 9500, S. C. de Bariloche, Rio Negro, 8400, Argentina*
[e] *UNIDEF, CONICET, MINDEF, Departamento de Investigaciones en Sólidos, CITEDEF, J.B. de La Salle 4397, B1603ALO Villa Martelli, Pcia. de Buenos Aires, Argentina*
[f] *ALBA Synchrotron Light Source, Carrer de la Llum 2-26, 08290 Cerdanyola del Vallès, Barcelona, Spain*
[g] *Department Structure and Dynamics of Energy Materials, HZB, Hahn-Meitner-Platz 1, 14109 Berlin, Germany*
[h] *Institute of Electrochemical Energy Storage, HZB, Hahn-Meitner-Platz 1, 14109 Berlin, Germany*
[i] *Institute for Solar Fuels, HZB, Hahn-Meitner-Platz 1, 14109 Berlin, Germany*
[j] *IET-1 Fundamental Electrochemistry, FZJ, Wilhelm-Johnen-Straße, 52428 Jülich, Germany*
[k] *Department of Chemistry and Pharmacy, Friedrich-Alexander-Universität Erlangen-Nürnberg (FAU), Egerlandstr. 3, 91058 Erlangen, Germany*
[l] *Department of X-ray Spectroscopy at Interfaces of Thin Films, Helmholtz Institute Erlangen-Nürnberg for Renewable Energy (HI ERN), Albert-Einstein-Str. 15, 12489 Berlin, Germany*

† Electronic supplementary information (ESI) available. See DOI: **https://doi.org/10.1039/d4ee02839b**

Broader context

Water electrolysis is crucial for effective harnessing energy coupling with intermittent renewable energy sources like wind and solar energy, being iridium the state-of-the-art anode catalyst for the sluggish oxygen evolution reaction (OER). However, its scarcity drives efforts towards low loading designs with high catalyst activities and low Ir dissolution rates, where the catalyst-specific activity-stability trade-off is particularly relevant. A preeminent candidate, amorphous, hydrous iridium oxide (am-hydr-IrO_x), exhibits higher activity but poorer stability compared to benchmark anhydrous rutile-IrO_2, urging for the understanding of the intricate relationship between these processes and for the atomistic description of the underlying (electro)chemical mechanisms. While mechanistic insights based on rutile-IrO_2 models have been proposed, these explanatory frameworks derived from highly ordered materials are insufficient for describing the amorphous and hydroxylated suboxide nature of the highly active am-hydr-IrO_x. In this study, we combine results derived from *in situ* and operando characterization techniques (*e.g.*, synchrotron-based X-ray spectroscopies) with density functional theory calculations to derive a comprehensive model that better describes the highly dimensional structure of am-hydr-IrO_x. The proposed theoretical approach is capable of disentangling the OER-limiting steps from the precious metal dissolution process and arises as an efficient model to better describe highly active, amorphous catalysts for water splitting.

Introduction

Water electrolysis (WE) is vital for global sustainable and renewable energy systems.[1] Efficient and stable anode materials for the oxygen evolution reaction (OER) are essential for the advancement of proton exchange membrane (PEM) WE technology, with iridium-based materials being state-of-the-art.[2,3] A preeminent OER candidate material is highly active amorphous, hydrous iridium oxide (am-hydr-IrO_x). However, its technological application is hindered by high iridium dissolution rates.[4,5] Thus, the realization of stable am-hydr-IrO_x based catalysts relies crucially on understanding the mechanisms underlying OER and Ir dissolution. Numerous studies have been devoted to deciphering activity-stability relationships in iridium oxides,[6–9] where the crystal structure was reported to strongly influence its properties, with am-hydr-IrO_x exhibiting superior OER activity but inferior stability compared to its crystalline-IrO_2 counterparts.[10–12] Complementary mechanisms have been proposed to explain the different OER performance of these two material classes,[13–17] namely: the adsorbate evolution mechanism (AEM)[18–20] and the lattice oxygen evolution mechanism (LOER).[21–23] These classical mechanisms describe transitions in the oxidation state (coordination) of the active Ir species during the 4-electron transfer process, with AEM prevailing in crystalline oxides and LOER in amorphous (hydrous) iridium oxides. For the latter, the participation of lattice oxygen in the OER mechanism is suggested to be directly related to the higher dissolution of Ir atoms, supposedly *via* unstable valent states,[24,25] which paved the way to the widely accepted entangled mechanism explaining the strong activity-instability correlation in these Ir oxides. Yet the use of crystal-based theoretical model interpretations[26–30] limits the ability to comprehensively describe iridium oxide variants without any long-range order, like am-hydr-IrO_x. The high structural complexity of these amorphous materials, linked to the presence of bulk defects, constitutes an insurmountable translational gap for these crystalline models, which we aim to address in this study.

Consequently, we investigated hydrous iridium oxide thin films (HIROFs) as a model system for am-hydr-IrO_x exhibiting a singular iridium suboxide species typically related to a high OER activity.[31–33] The complex structure of this hydroxylated porous electrochemically grown oxide requires appropriate theoretical models to interpret its OER activity and stability[4,33] beyond conventional crystalline-IrO_2 approaches. Furthermore, lack of long-range order necessitates the use of experimental techniques capable of probing the local electronic and geometric structural configurations of the material under relevant operational conditions. *In situ* X-ray absorption spectroscopy in combination with density functional theory (DFT) emerges as a suitable tool to unveil the complementary mechanisms governing the OER activity of am-hydr-IrO_x and its low stability caused by high Ir dissolution. Using an overarching dual-mechanistic theoretical framework, unique insights into Ir dissolution occurring already below the onset of OER, and the predicted high activity of electrophilic O-species[26,28–30,34,35] and metal Ir-sites are revealed and discussed in this study. The study's integrated approach offers a valuable methodology for understanding and optimizing OER and Ir dissolution mechanisms, thereby advancing the development of efficient and stable am-hydr-IrO_x-based anode materials.

Results

In situ synthesis of a highly porous am-hydr-IrO_x

This work studies the structure of am-hydr-IrO_x and its OER and Ir dissolution mechanisms by investigating hydrous iridium oxide thin film (HIROF) as a model system. HIROF is produced by the controlled electrochemical oxidation of a metallic Ir (Ir^0) substrate by continuous cycling between reductive and oxidative potentials, resulting in the monolayer-by-monolayer growth of am-hydr-IrO_x[31] (Fig. 1(a)). The fast oxidation kinetics coupled with slower reduction kinetics[36] during the rapid cycling results in the formation of highly porous, hydrated am-hydr-IrO_x with large number of bulk defects.[33,37] This '3-dimensional' electrocatalyst features a high density of catalytically active sites allowing for near-complete participation of all Ir atoms in redox reactions,[4,33] as indicated by the strong redox peaks in the pseudo-capacitive region of the cyclic voltammograms (CVs), increasing with the number of growth cycles (Fig. 1(b)). Interestingly, the double-layer region and hydrogen underpotential deposition (H_{UPD}) regions remain mostly unchanged during the growth, proportional only to the constantly accessible surface of the underlying metallic Ir substrate.[11,31,38] The am-hydr-IrO_x

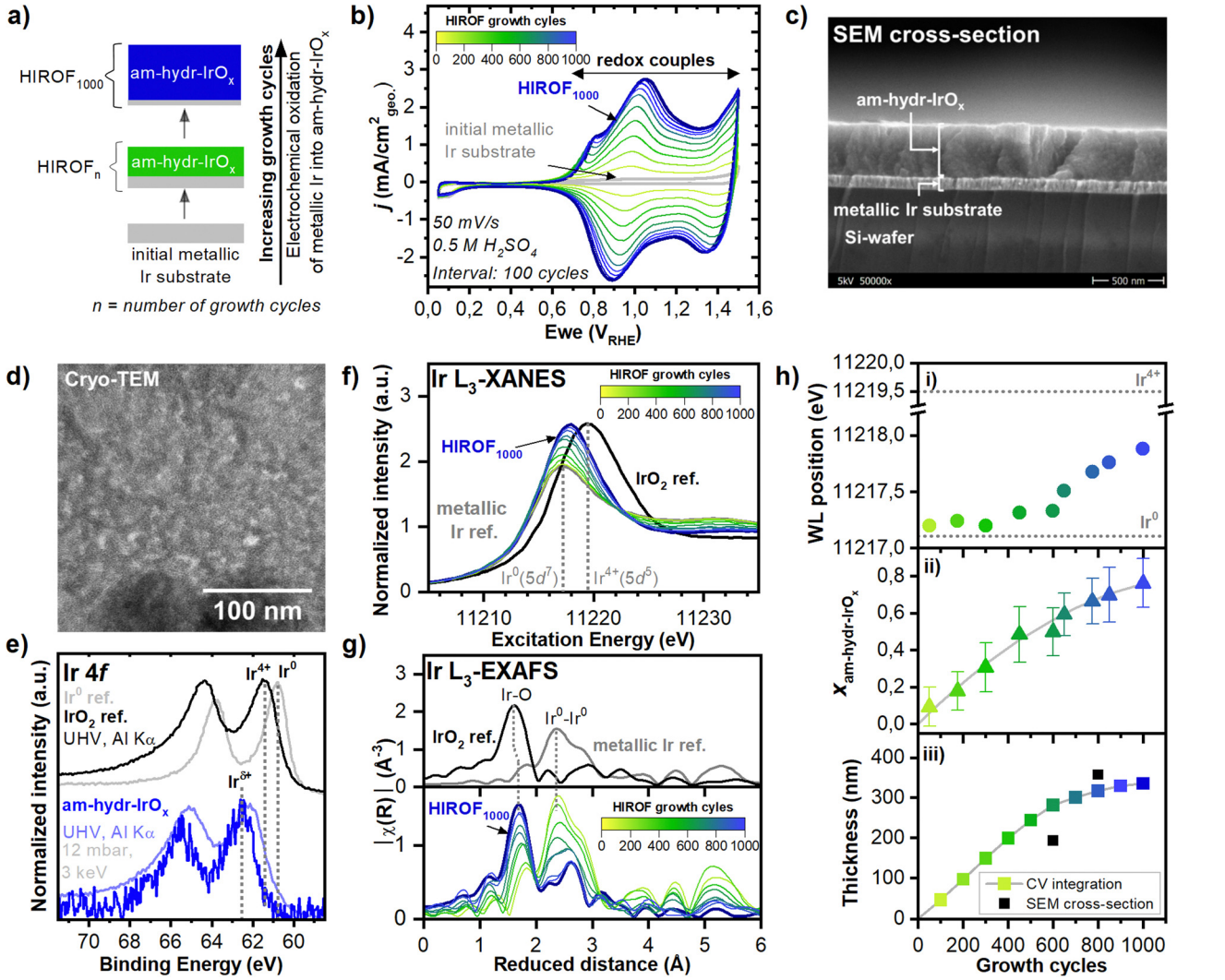

Fig. 1 Electronic synthesis and characterization of am-hydr-IrO_x. (a) Schematic of the electrochemical oxidation of Ir^0 into $HIROF_n$, where n is the number of growth cycles. (b) Cyclic voltammograms (CVs) acquired at intervals of 100 cycles at 50 mV s^{-1} during HIROF growth to 1000 cycles ($HIROF_{1000}$), exhibiting distinct redox processes. (c) Cross-section scanning electron microscopy (SEM) image of HIROF grown to 600 cycles from a 100 nm metallic Ir substrate. (d) Cryogenic transmission electron microscopy (cryo-TEM) image of am-hydr-IrO_x. (e) Ir 4f spectra of am-hydr-IrO_x obtained by Al K_α ultra-high vacuum X-ray photoelectron spectroscopy (UHV XPS, light blue) and *in situ* "dip-and-pull" near-ambient pressure hard X-ray photoelectron spectroscopy (NAP-HAXPES, dark blue) at 12 mbar using 3 keV, see Supplementary Notes 5 and 6 (ESI†), respectively, for further details. Spectra were normalized to the Ir $4f_{7/2}$ peak maximum. UHV XPS Ir 4f spectra of metallic Ir (Ir^0, grey), Ir $4f_{7/2}$ at 60.8 eV binding energy, and rutile-IrO_2 reference (Ir^{4+}, black), Ir $4f_{7/2}$ at 61.5 eV, is shown for comparison. The dotted vertical lines mark the maximum intensity of the $4f_{7/2}$ peaks. (f) *In situ* Ir L_3-edge X-ray absorption near edge structure (XANES) recorded at intervals during HIROF growth to 1000 cycles. Spectra of Ir^0 (grey) and rutile-IrO_2 (black) are shown as references for the white-line (WL) positions of Ir^0 and Ir^{4+}. (g) *In situ* k^2-weighted Fourier transforms (FTs) of the Ir L_3-edge Extended X-ray Absorption Fine Structure (EXAFS) recorded in intervals during the HIROF growth to 1000 cycles. Ir^0 (grey) and IrO_2 (black) references are shown for comparison, with vertical lines marking the 'Ir–O' and 'Ir^0–$Ir^{0'}$' first coordination shell scattering peaks. FT analysis highlights the unique local geometric structure of am-hydr-IrO_x (Ir–O scattering peak at longer bond lengths compared to rutile-IrO_2). (h) (i) *In situ* recorded Ir L_3-edge WL position, (ii) mole fraction determined from EXAFS fittings, and (iii) am-hydr-IrO_x film thickness determined by CV charge integration as a function of growth cycles. Horizontal dashed lines in (i) indicate the Ir^0 and rutile-IrO_2 reference WL positions. The solid grey line in (ii) indicates the fitted second-order polynomial trend line. Plotted in black squares in (iii) are the am-hydr-IrO_x film thicknesses determined from cross-section SEM images, for HIROF grown to 600 and 800 cycles.

layer acts as a switchable conductor, becoming active for anodic reactions (such as redox and OER) and inactive for cathodic reactions (like H_{UPD}), which are only characterized by the underlying metallic Ir substrate (see Fig. S1 in Supplementary Note 1, ESI†). The poor electronic transport of highly hydrated iridium oxides at potentials below 0.6 V_{RHE} is likely hindering the contribution of the evolving surface at this lower potential window. Cryogenic Transmission Electron Microscopy (cryo-TEM) ought to show the highly disordered nature of am-hydr-IrO_x measurements in its native acidic aqueous environment (Fig. 1(c)), responsible for its amorphous porous structure and low density[32] (~1–2 g cm^{-3} compared to $\rho_{rutile\text{-}IrO_2}$ = 11.6 g cm^{-3}, refer to Supplementary Note 2 for calculation details, ESI†). More details on the electrochemical behaviour of am-hydr-IrO_x as well as the

comparison with metallic Ir and rutile-IrO_2 can be found in Supplementary Note 3 (ESI†) and extensively elsewhere.[4,11,13,33]

The chemical nature of am-hydr-IrO_x was probed under hydrated conditions by ''dip-and-pull'' technique[39–41] *in situ* near ambient pressure hard X-ray photoelectron spectroscopy (NAP-HAXPES), which exhibited a single electronic state with a Ir 4f binding energy (BE) position higher than anhydrous rutile-IrO_2 and similar to that predicted for the trivalent Ir-defect site in rutile-IrO_2[26] (Fig. 1(d), and complementary O 1s spectra in Fig. S8 in Supplementary Note 4, ESI†). This observation aligns with previous studies on highly hydroxylated Ir(III)OOH nanosheets[42] and other am-IrO_x.[29,43] Under ultra-high vacuum (UHV) conditions, am-hydr-IrO_x exhibits a broader Ir 4f peak shape (light blue spectra in Fig. 1(d)) explained by a higher contribution of Ir^{4+} in the analytical fit and lattice-O in the O 1s spectrum (Fig. S11 in Supplementary Note 5, ESI†), associated with its (oxy)hydroxide nature (refer to Supplementary Notes 4 and 5 for more details of the analytical fits, ESI†). Presumably, UHV conditions cause dehydration[44,45] resulting in mixed iridium states (Fig. S12 in Supplementary Note 5, ESI†), whereas hydrated conditions preserve am-hydr-IrO_x's hydroxylated form in a single electronic state. This hydroxylated iridium suboxide species in am-hydr-IrO_x is of prime interest, as it has often been associated with sites with high intrinsic OER activity.[9,26] These catalytic sites involve coordinatively unsaturated electrophilic O-species situated at Ir defect sites.[26,29,30]

The electronic and local geometric structure of am-hydr-IrO_x was further investigated under hydrated conditions by means of bulk-sensitive *in situ* Ir L_3-edge X-ray absorption near-edge structure (XANES) (Fig. 1(e)) and extended X-ray absorption fine structure (EXAFS) measurements (Fig. 1(f)) during the growth of HIROF to 1000 cycles. The evolving XANES and EXAFS spectra confirm near-complete conversion of Ir^0 into am-hydr-IrO_x. Am-hydr-IrO_x exhibits an Ir L_3-edge white-line (WL) position at lower excitation energies than rutile-IrO_2 (Fig. 1(e) and (g)-(i)), confirming its unique suboxide state, consistent with our *in situ* NAP-HAXPES observations. Complementarily, Fourier transform (FT) analyses of the k^2-weighted Ir L_3-edge EXAFS spectra (Fig. S14, ESI†) reveal the unique geometrical structure of am-hydr-IrO_x (Fig. 1(f)). The evolving FT spectra (green to blue in Fig. 1(f)) reveal the conversion of the metallic Ir substrate (scattering peak at ~2.26 Å attributed to the first-shell Ir^0–Ir^0 in the metallic Ir reference) to am-hydr-IrO_x, with a characteristic Ir–O scattering peak at ~1.68 Å (blue spectra in Fig. 1(f)). This indicates that am-hydr-IrO_x has a longer Ir–O bond length compared to crystal rutile-IrO_2, which has an Ir–O scattering peak at ~1.61 Å. This demonstrates the distinctly different structure of am-hydr-IrO_x in comparison to rutile-IrO_2, which we consider as important as the Ir–O bond length is proposed to be a fundamental factor influencing OER activity.[46,47]

The characteristic, dominating spectral fingerprint of am-hydr-IrO_x after 1000 cycles of HIROF growth confirms its successful preparation with a thickness sufficient to dominate the Ir L_3-edge XAS spectroscopic signal. Quantitative analysis of the first-shell Ir^0–Ir^0 and Ir–O scattering paths in the EXAFS spectra (see Supplementary Note 6 for the fits of the EXAFS data, ESI†) was used to determine the molar fractions of the Ir^0 and am-hydr-IrO_x in the total generated HIROF sample after 1000 cycles. These analyses reveal an ~80% molar contribution of am-hydr-IrO_x in HIROF after 1000 cycles (Fig. 1(g)-(ii)), corresponding to a thickness of ~300 nanometres (Fig. 1(g)-(iii)), as calculated from charge integration of the main redox couple (refer to Supplementary Note 1 for CV integration details, ESI†) and cross-validated by cross-section SEM images. CVs reveal negligible differences in the characteristic features after ~800 cycles (Fig. 1(b)), pointing towards increased mass transport limitations within the film.[33] Continued growth beyond 1000 cycles is undesirable as this would lead to eventual am-hydr-IrO_x layer detachment due to mechanical instability.[48]

Our results collectively highlight the necessity for a revised structural model tailored to am-hydr-IrO_x, considering its unique electronic and structural properties (singular, hydroxylated Ir suboxide species, '3-dimensional' nature, high active site density, and longer Ir–O bond length) challenging the use of conventional rutile-IrO_2 based theoretical interpretations. Utilization of highly periodic structures would be unsuitable for modelling materials like am-hydr-IrO_x which exhibit only short-range order, and also possess some amount of defects. This also introduces the likelihood of a diverse array of distinct possible active sites associated with different chemical environments. Therefore, novel structures, more accurately representing the physicochemical properties of am-hydr-IrO_x, which dictate its OER behaviour, are required.

Revealing the structural configuration of am-hydr-IrO_x by theory-guided evaluation *of in situ* Ir L_3-edge XAS data

A comprehensive screening of structures that could model am-hydr-IrO_x was performed by comparing the experimental *in situ* Ir L_3-edge EXAFS data of $HIROF_{1000}$ with various atomistic models. These models range from more periodic rutile-types to flexible structures, with well-defined edges like stacked-sheets or nanosheets, potentially forming water containing ''hydrogel'' networks, similar to previous work on Ru oxides.[49] Given the highly porous nature, large surface area, and the monolayer-by-monolayer growth[31] of am-hydr-IrO_x, we expect highly flexible arrangements allowing for water intercalation to best describe am-hydr-IrO_x. For this reason, sheet-like structures have been proposed to complement the crystal-like periodic models. Providing enough lateral periodicity to mirror the short-range order observed experimentally, finite sheet structures offer a variety of local motifs at the edges that can mimic the defective environments and coordinatively unsaturated O-edge sites found in bulk vacant sites associated with high activity.[9,29] With sufficient size to bridge the mesoscale of the studied material with the computational limitations of current quantum chemistry, these nanosheets exhibit high mobility of charge carriers, allowing for good electronic and ionic transport in the material, as expected from a highly active OER electrocatalyst as am-hydr-IrO_x. For all the proposed models, various surface terminations (*e.g.*, *H, *O, *OH, *OOH, and their numerous combinations) and different degrees of surface coverages (Θ_i) were considered. All the structures have been pre-selected by *ab initio*

thermodynamics (*i.e.*, most stable structures from a large structural manifold with a formal theoretical basis for their existence).

Individual fits of the experimental EXAFS data were performed using every atomic model, constraining their interatomic distances and coordination numbers obtained after structural relaxation (see Supplementary Note 7 (ESI†) for details on the EXAFS fittings and on the figure-of-merit parameter – 1/*r*-factor – used to quantify the EXAFS goodness-of-fit). This systematic approach, focusing on EXAFS fitting of the short-range order, served as an efficient filter to select the most probable structure families and surface terminations to describe am-hydr-IrO_x. Fig. 2(a) shows the EXAFS goodness-of-fit of the different structure-termination-permutations considered, which describes their ability to mimic the elongated Ir–O bond of am-hydr-IrO_x.

Nanosheet structures exhibited the highest goodness-of-fit (largest circle in Fig. 2(a)), and thus is the best atomistic model to describe the structural properties of am-hydr-IrO_x, along with stacked-sheet structures. These results suggest a structured network composed of pores and channels, where single nanosheets likely describe the walls, and stacked sheets are indicative of the joints. This amorphous architecture likely facilitates efficient water transport between interconnected nanostructures, mirroring the highly porous structure of am-hydr-IrO_x. Nanosheets consist of hydrogen atoms adsorbed preferentially atop the threefold-coordinated O atoms (O^{3f}), which are bonded to sixfold-coordinated Ir atoms (Ir^{6f}) (Fig. 2(b)). At the nanosheet edges, coordinatively unsaturated Ir sites (Ir^{cus}) are present with O existing as both onefold-coordinated terminal (O^{cus}) species and as twofold-coordinated bridging O-atoms (O^{br}). These edge sites can be used as a proxy to simulate bulk defective environments likely found in am-hydr-IrO_x, which are also analogous to electrophilic μ_1-O and μ_2-O species in the Ir-defect site of the rutile-IrO_2 structural model as discussed elsewhere.[9,29,30,35] The optimal H-coverage (Θ_H) was determined to be 0.50 monolayer (ML) (Fig. 2(c) and (d)). Structural models

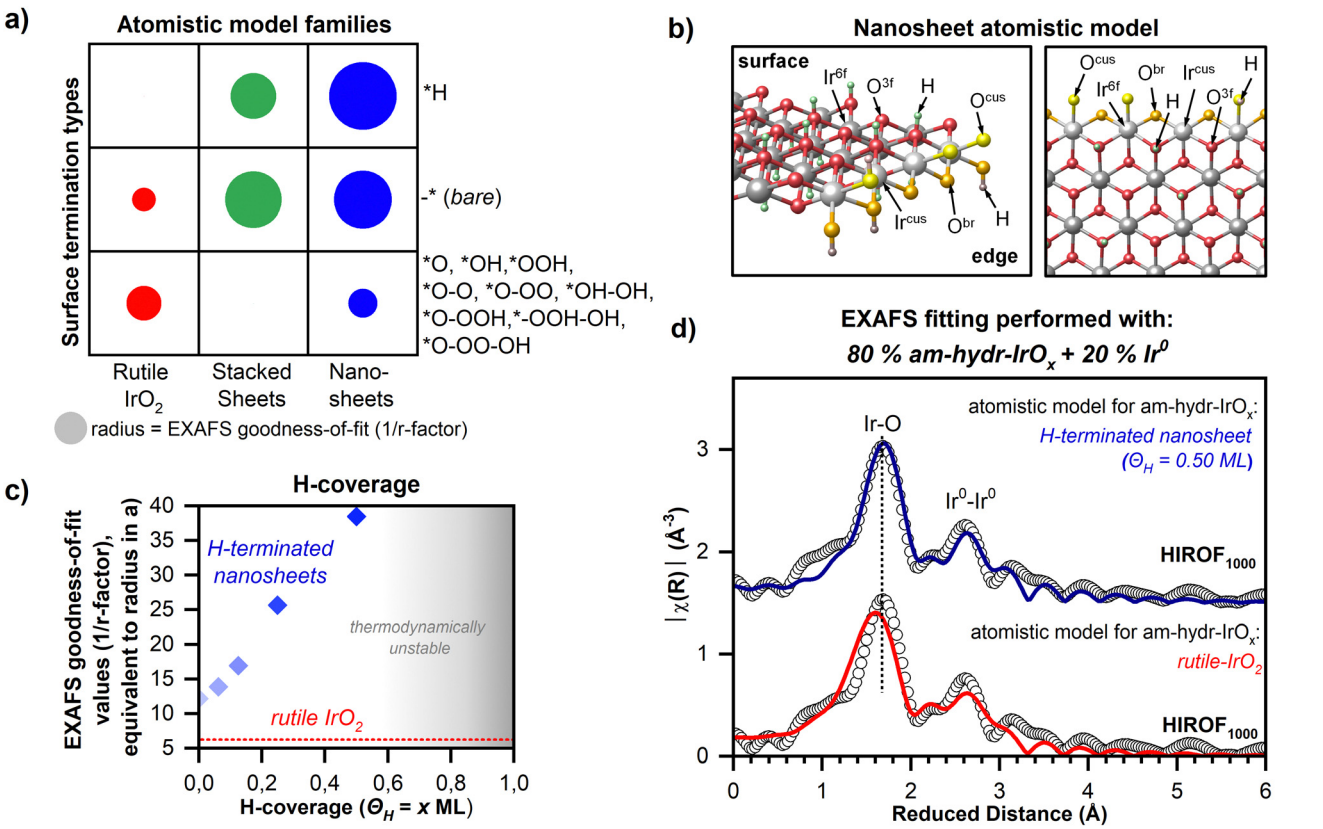

Fig. 2 Electronic and local geometric structure of am-hydr-IrO_x. (a) EXAFS goodness of fit values (1/*r*-factor from the EXAFS fit results) for a library of atomic models differentiated by atomic model families and surface termination types. Atomic model families include rutile-IrO_2, stacked sheets, and nanosheet structures. Surface termination types were divided into H-terminated, bare, and oxo, peroxo, superoxo groups. The radii of the circles correspond to goodness of EXAFS fit values. Overall, nanosheets describe the experimental data the best. See Supplementary Note 11 (ESI†) for more details of EXAFS fittings. (b) Ball and stick perspective and top model views of the nanosheet with a 0.50 monolayer H-coverage (Θ_H = 0.50 ML). The threefold-coordinated O^{3f} and sixfold-coordinated Ir^{6f} surface species constituting the nanosheet surface are highlighted. At the nanosheet edges, the coordinatively unsaturated (cus) Ir^{cus}, onefold-coordinated terminal O^{cus}, and twofold-coordinated bridging (br) O^{br} species are highlighted. (c) EXAFS goodness of fit values (1/*r*-factor from the EXAFS fit results) as a function of H-coverage (Θ_H) for EXAFS fits using nanosheet structures with varying H-coverages. (d) *in situ* k^2-weighted FT spectra of $HIROF_{1000}$ with EXAFS fits performed using an H-terminated (Θ_H = 0.50 ML) nanosheet structure (in blue) compared to employing the conventional bulk rutile (tetragonal) IrO_2 structure (in red) for the am-hydr-IrO_x component (molar fraction = 80%). Elemental fcc (face-centered cubic) Ir was used for the metallic Ir substrate component (molar fraction = 20%).

with higher Θ_H values were thermodynamically unfavourable, *e.g.*, undergoing Ir–O bond breaking during the structural relaxation; therefore, these models were not considered in the analysis of the experimental data. In fact, the low current densities measured at the double-layer region of the CV (Fig. 1(b)) likely originate from the low electronic conductivity typically associated with highly hydrated structures, as the nanosheet found to best fit our data. The use of the nanosheet atomistic model with Θ_H = 0.50 ML in the EXAFS fitting (Fig. 2(d)) illustrates its improved description of the electronic and structural properties of am-hydr-IrO_x in comparison with conventionally adopted rutile-IrO_2. This supports experimental observations by *in situ* NAP-HAPXES and *in situ* Ir L_3-edge XANES and EXAFS measurements (Fig. 1), highlighting the distinctly different chemical environment in am-hydr-IrO_x (*e.g.*, hydroxylated Ir suboxide and longer Ir–O bond, 2.04 Å) in comparison to rutile-IrO_2 (*e.g.*, anhydrous Ir^{4+} and shorter Ir–O bond, 1.98 Å). Our results bridge a critical gap in literature by unveiling the (until now) undefined structure of highly hydroxylated iridium suboxide materials, better describing the higher surface area and flexible morphology of am-hydr-IrO_x.

This advances our ability to investigate and understand the electronic and structural changes of am-hydr-IrO_x under potential application, providing a coherent theoretical–experimental framework to interpret the intricate mechanisms that define its OER electrocatalytic behaviour (*i.e.*, activity and stability). The unique structure of the nanosheet suggests the presence of various potential active sites (Ir^{6f}, O^{3f} and the edge-related Ir^{cus}, O^{cus} and O^{br} sites mimicking bulk defects) and thus hinting at the co-existence of multiple OER reaction pathways in am-hydr-IrO_x, beyond the commonly assumed mechanisms based on rutile-IrO_2 surfaces.[9,13,22,26,34,35] The following section aims to interpret the potential-induced transformations of am-hydr-IrO_x using this newly introduced H-terminated nanosheet model.

Electronic and structural transformations of am-hydr-IrO_x under potential application

Electronic and structural changes of am-hydr-IrO_x under potential application were investigated by *operando* Ir L_3-edge XANES and EXAFS, along with Fixed Energy X-ray Absorption Voltammetry (FEXRAV),[50] with three distinct regimes: "pre-redox", "redox" and "OER" (Fig. 3).

At potentials ($< \sim 0.60$ V_{RHE}), characterized by near-featureless CV response indicating minimal charge transfer processes, am-hydr-IrO_x exhibits subtle changes in its electronic and structural configuration, evidenced by a slight WL shift (Fig. 3(a)) and minor changes in its Ir–O bond length (Fig. 3(c)).

A more significant WL shift occurs between ~ 0.60 V_{RHE} and ~ 1.23 V_{RHE} (Fig. 3(a)). This potential region is typically attributed to a $Ir^{3+} \leftrightarrow Ir^{4+}$ redox couple with a maximum around 0.97 V_{RHE} and a smaller pre-peak at 0.70 V_{RHE} with various attributions[51,52] (Fig. 3(b)). The potentiodynamic FEXRAV measurement (orange curve in Fig. 3(a)), which monitors the spectral intensity change at a fixed excitation energy of 11219.5 eV (WL of rutile-IrO_2) during cyclic voltammetry,[50] provides insights into the reversibility of the main redox

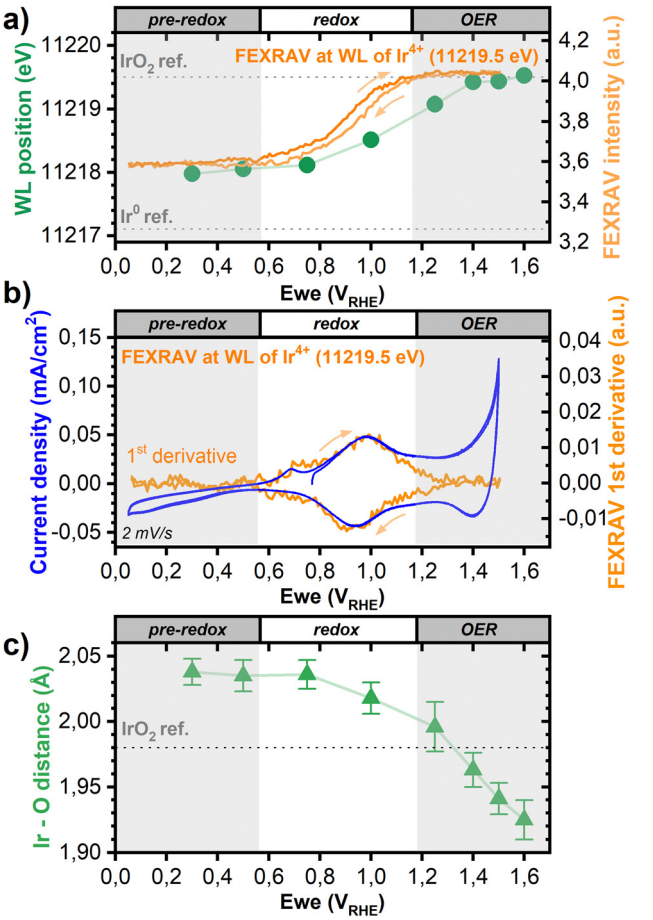

Fig. 3 Electronic and local geometric structural transformation of am-hydr-IrO_x under potential application. (a) *Operando* Ir L_3-edge white-line (WL) position as a function of applied potential. Horizontal dashed grey lines indicate the Ir^0 and rutile-IrO_2 reference WL positions. Fixed energy X-ray voltammetry (FEXRAV) measurement at the WL position of Ir^{4+} (11219.5 eV) is shown in orange in (a) and in (b) its corresponding CVs acquired at 2 mV s^{-1} is shown in blue. The FEXRAV 1st derivative is shown in orange in (b). (c) First coordination shell Ir–O distance of am-hydr-IrO_x as a function of applied potential, obtained by *operando* Ir L_3-edge EXAFS fits using the H-terminated nanosheet (Θ_H = 0.50 ML) structure. The horizontal dashed grey line indicates the first coordination shell Ir–O distance of the rutile-IrO_2 reference.

couple, associated with the first major electronic transformation of am-hydr-IrO_x. The FEXRAV 1st derivative signal (orange line in Fig. 3(b)) closely aligns with the oxidation/reduction profiles of the main redox peak (blue line in Fig. 3(b)), highlighting the reversibility of the oxidation/reduction process. Furthermore, the Ir–O bond length also starts to decrease within this regime (Fig. 3(c)).

A third distinctive region is observed under OER relevant potentials (>1.23 V_{RHE}), where the WL energy position does not significantly change but a stronger contraction of the Ir–O bond length is evident (Fig. 3(c)).

The observed trends in the WL position shifts and Ir–O bond length contraction of am-hydr-IrO_x agree with the trends found in other studies on amorphous iridium oxides,[53–59] however, limited interpretations of their electronic behaviour are

provided, and mainly based on rutile-IrO_2 models. Our alternative approach, using the highly dimensional, amorphous and flexible H-terminated nanosheet model, establishes a dual-mechanistic theoretical framework based on DFT-predicted structural transformations of the nanosheet (Fig. 4). The proposed model supports the experimental WL position and Ir–O bond length data trends of am-hydr-IrO_x and attempts to unify in a unique explanatory framework the dissolution of Ir with the oxidation behaviour extensively observed in the redox and OER regions, thereby providing deeper insights into the electronic and structural transformation processes occurring across the three potential regions and the correlations between both mechanisms.

Dual-mechanistic framework: chemical transformations and spontaneous Ir dissolution

Ab initio thermodynamic analysis was employed to reveal the structural progression of the nanosheet with changing

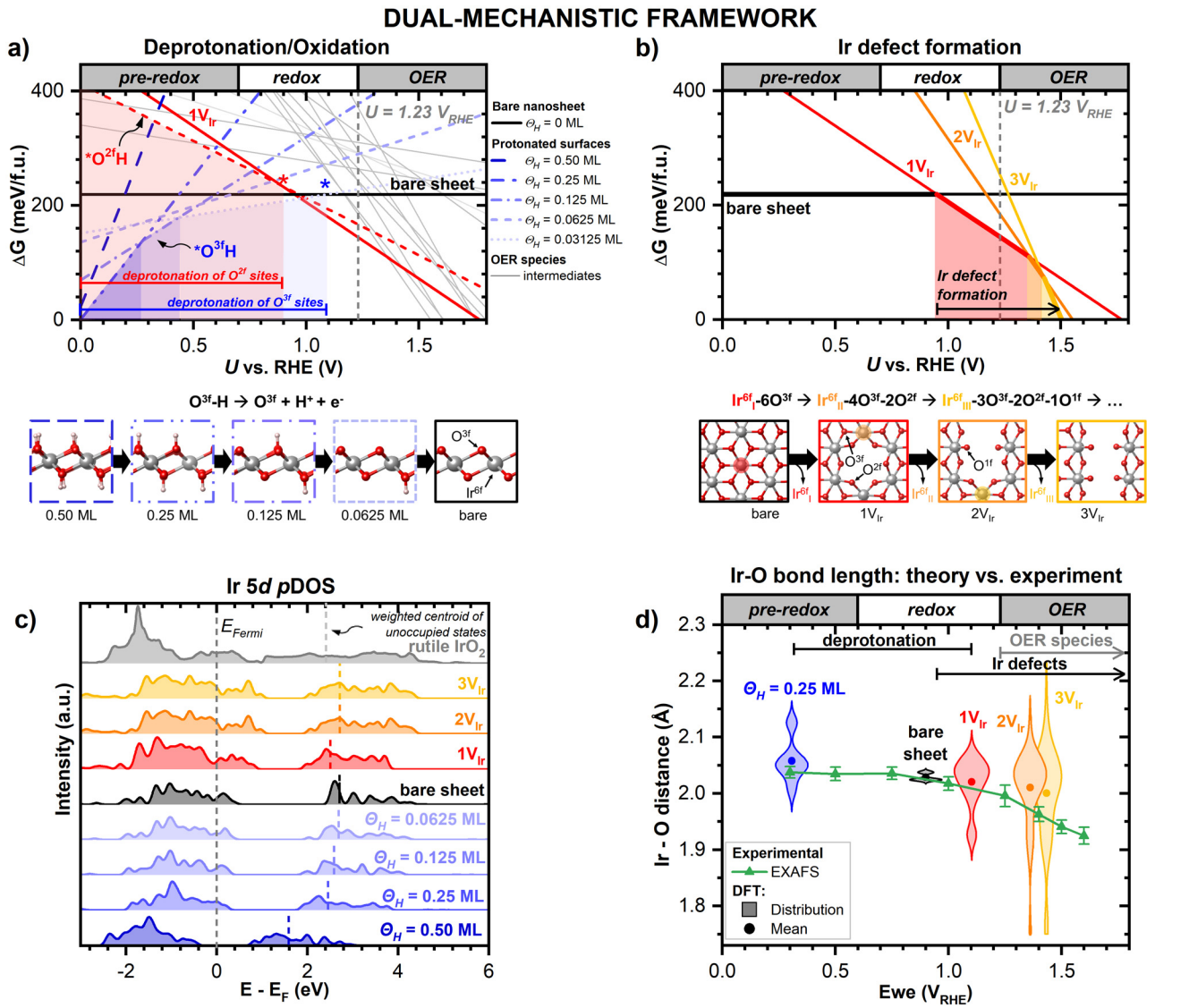

Fig. 4 DFT supported analysis of the *in situ* Ir L_3-edge XAS of am-hydr-IrO_x at applied potentials. (a) and (b) Phase diagrams showing the stability of the different terminations of the iridium nanosheet surface as a function of applied potential, following the dual-mechanism framework of (a) the chemical behaviour (*i.e.*, deprotonation and oxidation) and (b) Ir defect formation. The vertical dotted lines indicate the OER thermodynamic equilibrium potential of U = 1.23 V. At the top of each of the plots are marked the potential regions associated with the pre-redox, redox and OER regimes. Perspective atomistic views of the deprotonation of the nanosheet (Θ_H = 0.50–0 ML) and spontaneous Ir dissolution ($1V_{Ir}$, $2V_{Ir}$, to $3V_{Ir}$) in the nanosheet are shown under (a) and (b), respectively, highlighting the fully coordinated Ir^{6f} and O^{3f} species, and dangling O^{2f} and O^{1f} species. (c) Ir 5d derived partial density of states (pDOS) of the most stable structures predicted by the phase diagrams in (a) and (b). For comparison, the pDOS of rutile-IrO_2 is also shown. Vertical dashed lines give the energy position of the weighted centroid of the unoccupied states. (d) Comparison of the experimental and theoretical Ir–O interatomic distances. The *operando* experimental Ir–O bond lengths are reproduced from Fig. 3(c) and are shown as green triangles with error bars. DFT obtained distributions of Ir–O bond distances from the most stable structures predicted by the phase diagrams are shown by the coloured violin plots. The respective mean values are shown as circles. Black bars delimit the potentials related to the most relevant chemico-structural changes of am-hydr-IrO_x.

applied potentials. DFT-calculated phase diagrams (Fig. 4(a) and (b)) illustrate the nanosheet structures' Gibbs free energy of formation (ΔG) *versus* electrode potential, with lower ΔG indicating more thermodynamically favourable structures. Within the proposed dual-mechanistic framework, our analysis juxtaposes Fig. 4(a) the chemical transformations of the nanosheet in the pre-redox and redox potential regions, and Fig. 4(b) the spontaneous loss of iridium atoms from am-hydr-IrO_x during OER and at lower applied potentials. For this, Fig. 4(a) focuses on the chemical behaviour (deprotonation and oxidation), crucial for understanding the structural changes under redox potentials and insights into the distinct OER activity of the different sites co-existing in am-hydr-IrO_x. Complementary, Fig. 4(b) presents structures related to Ir defect site formation within the pristine nanosheet. Combined, Fig. 4 encapsulates the dual-mechanistic framework providing theoretical interpretations of the activity-stability trade-off in am-hydr-IrO_x.[4,11,33] Inherent bulk defects in am-hydr-IrO_x are modelled by the finite nanosheet edges. Moreover, a small quantity of Ir defects is expected during HIROF growth, given notable Ir dissolution quantities within this potential region (>1 V_{RHE}).[4,11,33] Their contribution to deprotonation behaviour is modelled using a nanosheet with a single Ir vacant site, *i.e.*, $1V_{Ir}$. The vertical lines at U = 1.23 V_{RHE} mark the thermodynamic OER onset potential.

Fig. 4(a) illustrates the DFT-predicted progressive deprotonation of distinct O-sites in the nanosheet, reaching complete deprotonation at high redox-relevant potentials. According to the reaction:

$$*O\text{–}H \rightarrow *O + H^+ + e^-$$

fully coordinated O^{3f} sites at the nanosheet's surface are progressively deprotonated from a Θ_H = 0.5 ML H-coverage until Θ_H = 0 ML coverage is reached at $\sim$1.10 V_{RHE}, indicated by the blue asterisk in Fig. 4(a), where the bare nanosheet (black horizontal line) intersects with nanosheets with H-surface coverages (blue lines). Similarly, complete deprotonation of the coordinatively unsaturated O^{2f} sites at Ir defect sites ($1V_{Ir}$) occurs already at slightly lower potentials within the redox region, $\sim$0.90 V_{RHE} (red asterisk in Fig. 4(a)). As previously reported by DFT calculations for rutile-IrO_2,[60,61] as the potential increases, the formation of key OER absorbed intermediate species (–OH, –OOH, and –OO) becomes increasingly likely. OER intermediates on all the plausible active sites in the nanosheet atomistic model, were considered (grey lines in Fig. 4(a)). Generation of higher oxidized intermediates is only favoured at OER potentials, according to the thermodynamic model described above. The higher ΔG of the proposed intermediates compared to the bare nanosheet within the redox potential region precludes their contribution to redox couple mechanisms. Our thermodynamic calculations strongly suggest deprotonation of both O^{2f} and O^{3f} as the major mechanism during the redox process within the region 0.4–1.2 V_{RHE}, and thus, challenges the extensively proposed Ir hydroxylation mechanism associated with the main redox couple.[32,48,62,63] Furthermore, the different deprotonation potentials of the saturated and unsaturated O-sites in the nanosheet ($\sim$0.90 V_{RHE} and $\sim$1.10 V_{RHE}) likely model the different chemical environments found in the grown am-hydr-IrO_x, reflecting the broad nature of the redox peak.

Considering the second aspect of the dual-mechanistic framework, *i.e.*, the structural transformations of the nanosheet, our DFT-guided study suggests that the formation of Ir defect sites:

$$Ir_I^{6f}\text{-}6O^{3f} \xrightarrow{Ir_I^{6f}} Ir_{II}^{6f} - 4O^{3f}\text{-}2O^{2f} \xrightarrow{Ir_{II}^{6f}} Ir_{III}^{6f}\text{-}2O^{3f}\text{-}2O^{2f}\text{-}1O^{1f}$$

in the bare nanosheet becomes thermodynamically favourable already below 1.23 V_{RHE} (at $\sim$0.95 V_{RHE}, intersection of black and red lines in Fig. 4(b)), prior to the formation of any expected higher-oxidized reaction intermediates. Our DFT calculations indicate losing an iridium atom from the nanosheet is a spontaneous, thermodynamically driven process, and unrelated to OER pathways, disagreeing with current proposed relationships between Ir dissolution and OER mechanisms.[13,64] The DFT-predicted $\sim$0.95 V_{RHE} onset potential for spontaneous Ir vacancy formation also coincides with the redox regime where deprotonation occurs (Fig. 4(a)), highlighting the co-existence of multiple processes occurring in this region and shedding light on reversible (main peak) and irreversible (pre-peak) redox features. This can also explain the high density of Ir defect sites in am-hydr-IrO_x likely due to Ir dissolution occurring during HIROF growth, a process involving repeated cycling around the potentials where spontaneous Ir vacancy formation is proposed. At even higher potentials, under OER relevant conditions, multiple adjacent Ir vacant sites (*e.g.*, $2V_{Ir}$ and $3V_{Ir}$) become rapidly more energetically favourable (Fig. 4(b)). Our DFT framework predicts a higher thermodynamic instability of the nanosheet structures within the OER region, and therefore exhibits robust alignment with experimentally observed high rates of Ir dissolution under OER conditions in am-hydr-IrO_x, as reported elsewhere.[4,11] The spontaneous dissolution of adjacent Ir atoms generates defective environments in the structure that resemble the local motifs already present in the sheet's edges and enhance the amount of coordinatively unsaturated oxygens. Our approach reveals that the progressive evolution of the nanosheet in the OER potential region is essential for creating new defect sites, though it comes at the cost of irreversible loss of iridium.

Assuming that the nanosheet atomistic model best describes the electronic and structural properties of am-hydr-IrO_x, our DFT-predicted dual-mechanistic framework provides explanatory theories for both chemical transformations (deprotonation and OER intermediate formation) and Ir dissolution processes, and is to the best of our knowledge, the first atomistic model able to describe the process of pronounced Ir dissolution at OER potentials. Based on these premises, this framework predicts several mechanisms (*e.g.*, deprotonation, Ir dissolution and oxidation) occurring with the three potential regions (pre-redox, redox and OER), which align well with the potential-dependent electronic and structural transformations of am-hydr-IrO_x

observed experimentally by *operando* Ir L_3-edge XANES and EXAFS (Fig. 3).

Beyond using the simplified average Ir oxidation state formalism often adopted in several studies,[8,65,66] interpretations of the experimental WL shifts (*e.g.*, electronic transformations of am-hydr-IrO_x) presented in this work are based on calculations of the Ir 5d partial density of states (pDOS) (Fig. 4(c)), which correlate with energy reconfigurations of the unoccupied states as probed by the XAS process. This approach avoids assumptions of one-to-one linearity between Ir L_3-edge WL position and formal Ir 5d occupancy describing Ir oxidation states, but rather interprets WL position shifts relative to modifications of the Ir 5d energy configurations with respect to the whole electronic structure. Further details on the correlation between the formal oxidation state of the active sites derived from simple electron-counting and the calculated electronic structure (based on the Bader charge analysis) are presented in Supplementary Note 8 (ESI†). O 2p pDOS are shown in Fig. S18 (ESI†) for completeness, although strong Ir–O hybridization in the nanosheets suggests similar trends to those observed in Ir 5d pDOS.

Interestingly, the expected low electronic conductivity of highly hydrated oxides could explain the insulating properties of am-hydr-IrO_x at low applied potentials *e.g.*, why at cathodic potentials the electrochemical signal is dominated by the underlying metallic Ir substrate (Fig. 1(b)). In the nanosheet structures with high H-coverages (*e.g.*, Θ_H = 0.50 ML in Fig. 4(c)), there appears a large gap in the Ir 5d pDOS, indicating insulating behaviour. As H-coverage decreases with increasing applied potential, the gap closes and Ir 5d states extend across the Fermi level, giving transition to a more conductive state.

The experimentally determined average Ir–O bond lengths obtained by EXAFS fittings correlate well with the trend of the different Ir–O bond lengths of the DFT-predicted nanosheet structures over the three potential regions (bond length distributions presented as violin plots in Fig. 4(d)).

In the pre-redox region below $\sim$0.60 V_{RHE}, characterized by minimal charge transfer processes, the experimental average Ir–O bond length (Fig. 3(c)) closely aligns with the DFT-predicted mean Ir–O bond lengths of the H-terminated nanosheet (Fig. 4(d)), longer than those of rutile-IrO_2. Likewise, the difference in the WL position of am-hydr-IrO_x and rutile-IrO_2 (Fig. 3(a)) agrees well with the anticipated difference in their Ir 5d electronic configurations. Analysis of the Ir 5d pDOS reveals a large difference in the energy positions of unoccupied states between the H-terminated nanosheet and rutile-IrO_2 (Fig. 4(c)), thus validating their large WL position difference.

The strong WL position shift over the redox regime (Fig. 3(a)) can be explained by the dramatic change of the electronic configuration as the H-terminated nanosheet becomes fully deprotonated. The trend in the large shift of the centroids of the Ir 5d unoccupied states towards higher energies following the deprotonation process (vertical lines in Fig. 4(d)) correlates well with the observed Ir L_3-edge WL position shift over $\sim$0.80 to 1.60 V_{RHE}. The centroids of the Ir 5d unoccupied states of the bare nanosheet and rutile-IrO_2 appear similar, confirming their expected similar Ir L_3-edge WL positions. Both experimentally observed WL position shift and initial Ir–O bond contraction (Fig. 3(a)) agree with the nanosheet structural transformation during deprotonation, culminating at the end of the redox potential region (Fig. 4(d)). The effect of a single Ir vacancy formation on the expected WL position is of roughly the same order of magnitude as arising from deprotonation (Fig. 4(c)). This further highlights the difficulty to deconvolute co-existing mechanisms in the redox regime and supports the need for a dual-mechanism to comprehensively explain the am-hydr-IrO_x behaviour.

Moreover, the rapid decrease in the experimentally observed Ir–O bond length within the redox and OER potential regimes aligns well with the DFT-predicted potential range for multiple Ir vacancy site formation. The $1V_{Ir}$, $2V_{Ir}$, and $3V_{Ir}$ nanosheet structures exhibit wide distributions of Ir–O bond lengths (Fig. 4(d)), with the shorter bonds emerging from edge termination effects and dangling bonds at the Ir defect sites (refer to Supplementary Note 9 (ESI†) for the different contributions of Ir–O bond distributions). Consequently, the observed reduction in Ir–O bond length can be related to (increasing) concentration of dangling bonds and edge terminations resulting from Ir vacancy site formation. Contraction of the Ir–O bond length increases with increasing OER potentials. In this potential regime, Ir defect site formation and formation of oxidized OER intermediates both influence Ir–O bond lengths.

Our dual-mechanistic DFT-guided framework (Fig. 4) reliably predicts the observed electronic and structural transformations of am-hydr-IrO_x across the pre-redox, redox, and OER potential regions, convincingly explaining trends in the shifts in the Ir L_3-edge WL position shifts and EXAFS determined Ir–O bond length contraction (Fig. 3). Thus, our study provides, for the first time, a comprehensive framework that can simultaneously explain all aspects of the activity-stability trade-off in am-hydr-IrO_x.

In the following section, we delve into the exploration of the different chemical environments that could participate in the OER to gain more insights into the underlying mechanisms in am-hydr-IrO_x.

DFT-guided understanding of the OER mechanism of am-hydr-IrO_x

The previous section outlined the DFT-predicted dual-mechanistic structural progression, suggesting that under OER potentials, finite nanosheets with highly accessible surface Ir^{6f} and O^{3f} sites, and coordinatively unsaturated O^{cus} and O^{br} edge sites (mimicking bulk defects) undergo Ir dissolution resulting in the formation of multiple Ir defect sites with additional coordinatively unsaturated O^{2f} and O^{1f} sites. These unsaturated O-sites have already been proposed to be responsible for the high activity of amorphous, hydrous iridium oxides.[8,29,30,35]

Supported by *ab initio* calculations and employing the widely adopted OER pathway,[67] our investigation primarily seeks to explore the underlying chemistry of each of these sites in the

nanosheet to unveil the nature of the OER mechanism(s) in am-hydr-IrO_x.

According to the classic DFT peroxide pathway proposed by Rossmeisl *et al.*,[67] the reactions can be described as follows for the O (*e.g.*, $O^{3f/2f/1f}$) and Ir (*e.g.*, Ir^{6f}) active sites:

$$\text{O-site: } {}^*O + H_2O \rightarrow {}^*O{-}OH$$

$$\xrightarrow{O_2} [Ir^{cus}]^* + H_2O \rightarrow {}^*O{-}H \rightarrow {}^*O$$

$$\text{Ir-site: } {}^*\underline{Ir} + H_2O \rightarrow {}^*Ir{-}OH \rightarrow {}^*Ir{-}O + H_2O$$

$$\rightarrow {}^*Ir{-}OOH \xrightarrow{O_2} {}^*Ir$$

where the charge carrier (H^+/e^-) balance is implicit and the catalyst resting state is underlined, constituting the starting reaction coordinate. The functional group (*i.e.*, *O or *Ir) is separated from the site by a "-_", and in the case of the bare site (*e.g.*, "*") the underlying site is denoted between "[]" (*e.g.*, $[Ir^{cus}]^*$). The sites explored in this work include the readily accessible surface Ir^{6f} sites, O^{1f} sites at Ir defect sites (modelled by $2V_{Ir}$ and $3V_{Ir}$) likely arising from Ir dissolution, and O^{cus} sites at nanosheet edges absorbed to Ir^{cus} sites, which mimic bulk defects. For the various plausible active sites in the nanosheet, only the edge site has a different resting state and its corresponding reaction is:

$$\text{Edge-site: } {}^*\underline{O{-}H} \rightarrow {}^*O + H_2O \rightarrow {}^*O{-}OH$$

$$\xrightarrow{O_2} [Ir^{cus}]^* + H_2O \rightarrow {}^*O{-}H$$

Fig. 5 illustrates the DFT-predicted thermodynamic stabilities of these OER intermediates (Fig. 5(a)) and their subsequent ΔG barriers for O_2 evolution alongside the marked potential

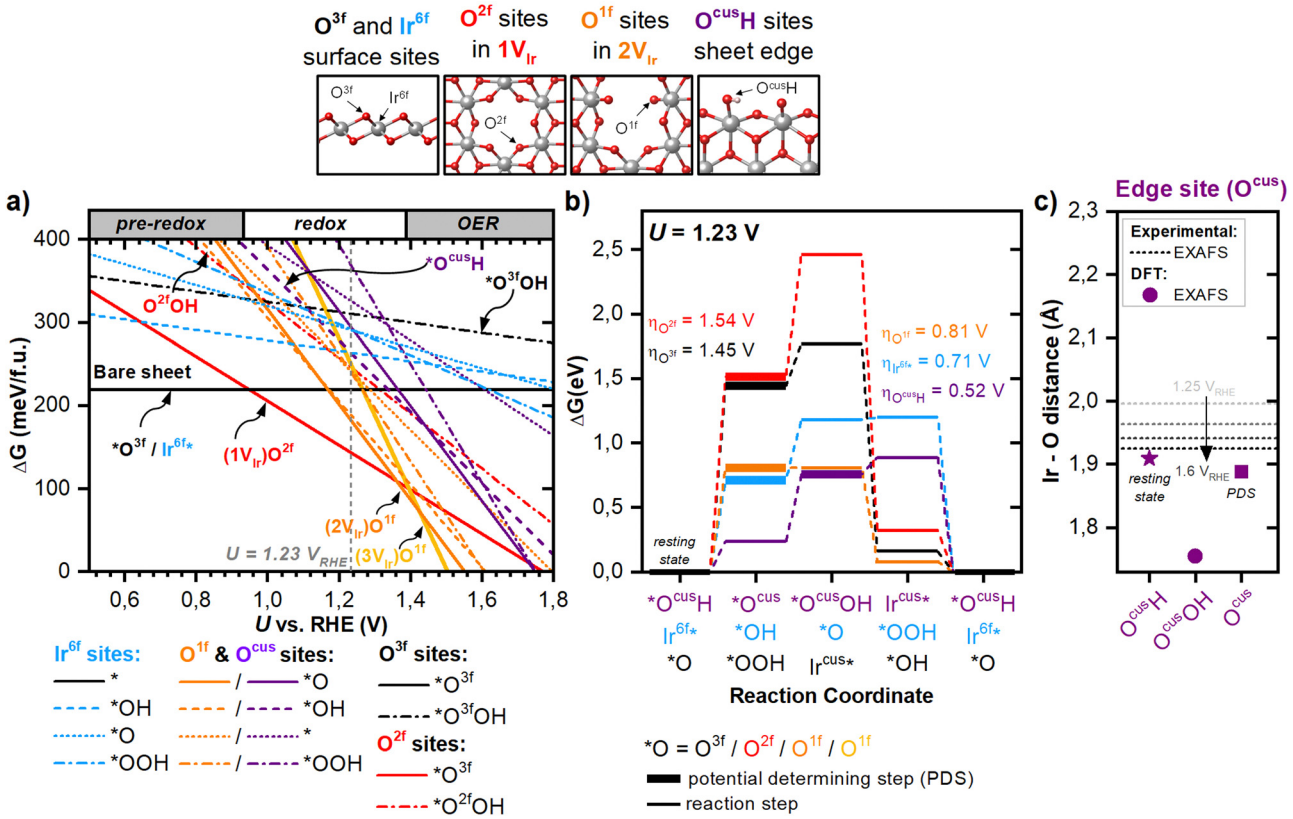

Fig. 5 DFT peroxide OER mechanism at multiple active sites within the nanosheet atomistic model. The top panels show the different active sites for which the energy requirements of the peroxide pathway were calculated: the O^{3f} and Ir^{6f} sites at the nanosheet surface, O^{2f} sites at the $1V_{Ir}$ defect sites, O^{1f} sites at $2V_{Ir}$ defect sites, and $O^{cus}H$ sites at the nanosheet edges. (a) Phase diagram showing the stability of different terminations of the nanosheet surface as a function of applied potential. The bare nanosheet with O^{3f} and Ir^{6f} sites is shown by the solid horizontal black line in the phase diagrams. Intermediate OER species (*O, *OH, *OOH, *—) at the coordinatively saturated Ir^{6f} sites are shown in blue, those at the coordinatively unsaturated O^{2f} site in the $2V_{Ir}$ atomistic model are shown in orange, and those at the O^{cus} edge site are shown in purple. The coordinatively saturated O^{3f} site with an *OOH ($*O^{3f}OH$) termination is shown by the black dashed line. The thermodynamic stability of the $3V_{Ir}$ structure is shown in yellow. The vertical dashed line indicates the OER thermodynamic equilibrium onset potential U = 1.23 V, and the potentials regions associated with the pre-redox, redox and OER regimes are marked at the top of the plot. (b) The reaction coordinate energy diagram for each active site is shown at U = 1.23 V, along with the reaction steps below. The potential determining step (PDS) indicates the highest free energy change and is indicated by the thicker lines. The thermodynamic overpotential (η) for each pathway is annotated in the energy diagram. (c) Comparison of the experimental Ir–O bond lengths derived from EXAFS fittings and the theoretical Ir–O interatomic distances of the OER intermediate species for the edge site ($O^{cus}H$). Horizontal lines indicate the experimental Ir–O bond lengths within the OER region (1.25–1.6 V_{RHE}). The resting state (most thermodynamically stable) is shown by the star and the PDS is indicated by the square.

determining step (PDS) (Fig. 5(b)) for the various potential active sites (Ir^{6f}, O^{3f}, O^{2f}, O^{1f} and O^{cus}). Oxygen vacancies ($[Ir^{cus}]$*) have not been included since their DFT-predicted ΔG at relevant potentials are much higher than the considered motifs without O-defects (Fig. S25 in Supplementary Note 10, ESI†). The most stable structure (*i.e.*, catalyst resting state) among reaction intermediates at each of the sites at 1.23 V_{RHE} (lowest ΔG) constitutes the starting reaction coordinate (Fig. 5(a)). The PDS describes the largest ΔG change among all four proton-coupled electron transfer (PCET) steps, which is the minimum required for OER to become exergonic (Fig. 5(b)). The prospective likelihood of the chemical species to act as active sites in am-hydr-IrO_x is evaluated based on their thermodynamic favourability and energy barriers of O_2 generation pathways using the nanosheet atomistic model.

Based on this theoretical framework, at 1.23 V_{RHE}, coordinatively unsaturated O-species (O^{1f} at Ir defect sites and O^{cus} at edge sites) are the most thermodynamically favourable sites for water oxidation (purple and orange lines in Fig. 5(a)). Surprisingly, atop site of fully coordinated Ir^{6f} is more thermodynamically favourable for the stabilization of higher oxidized OER intermediates (blue lines in Fig. 5(a)) than higher coordinated O-species (*i.e.*, O^{3f} and O^{2f}) showing higher ΔG values at 1.23 V_{RHE}. Fully coordinated O^{3f} atoms arise as the least reactive site, even compared to O^{br} or O^{cus} sites in rutile-IrO_2 surfaces.[60,61] Likely, the rigid, upstanding bond character of $*O^{3f}$–OH and their even distribution hinders the additional stabilization effects through hydrogen bond networks (large ΔG difference between $*O^{3f}$–OH and bare nanosheet lines in Fig. 5(a)).

Consequently, O^{3f} and O^{2f} sites exhibit the highest energy barriers for OER, with the first reaction steps of nucleophilic H_2O attack having the highest free energy changes of η = 1.45 V_{RHE} and η = 1.54 V_{RHE}, respectively (Fig. 5(b)). At the cost of irreversible Ir loss leading to the formation of multiple adjacent Ir vacant sites, highly uncoordinated dangling O^{1f} bonds at Ir^{cus} defect sites are one of the most energetically favourable OER sites (*e.g.*, orange $2V_{Ir}$ lines in Fig. 5(a)), with η = 0.81 V_{RHE} (Fig. 5(b)). Simulating finite structures like the studied nanosheets in this work offers a unique advantage in modelling the edge sites' contributions to OER (*i.e.*, mimicking bulk defects). The mixture of $*O^{cus}$–H/$*O^{cus}$ edge sites (Fig. S30 in Supplementary Note 10, ESI†) exhibited the lowest energy barrier for OER (η = 0.52 V_{RHE}, Fig. 5(b)) of all the investigated O-sites, consistent with findings on RuO_x nanosheets.[49]

While untangling contributions of parallel mechanisms to describe the experimentally measured average Ir–O bond length under OER potentials is challenging (given predicting kinetic effects with DFT is error-prone), comparing the theoretical and experimental Ir–O bond lengths already provides some insights into the potential dominating active sites and/or OER intermediates which best fit the experimental data. For instance, *O–H ($*O^{1f/cus}$–H) and *O–OH ($*O^{1f/cus}$–OH) species at the $O^{1f/cus}$ sites best agree with the experimentally observed Ir–O bond lengths at OER potentials. These two species represent the thermodynamic resting state (*O–H) and potential determining step (*O–OH), which according to the reaction scheme, would be present with highest concentrations given their lower energy barriers compared to the other reaction steps. These theoretical Ir–O bond lengths correlate well with the average Ir–O bond length observed experimentally (Fig. 5(c)), and further support the validity of our theoretical framework.

Our DFT calculations suggest OER-active sites in am-hydr-IrO_x extend beyond only the participation of O-sites – a perspective that has not previously been considered or integrated into current mechanistic schematics of OER.[13,35,68] Metal Ir^{6f} surface sites also offer a highly feasible O_2 formation pathway with η = 0.71 V_{RHE} (Fig. 5(b)). Activation of these sites occurs at much higher OER potentials, implying Ir participation in OER likely occurs at higher potentials (hinted by the additional small shift of the WL position $>$1.55 V_{RHE}), complementing current theories of a different OER and Ir dissolution mechanisms at higher potentials.[64,69]

While oxidation of edge sites is less thermodynamically favourable than generating Ir defect sites in the nanosheet (higher ΔG of purple edge *versus* orange defect lines at 1.23 V_{RHE} in Fig. 5(a)), edges and bulk defects are inherent in am-hydr-IrO_x due to the nature of HIROF preparation. Therefore, alongside highly active Ir defect site, O^{1f} bonds and surface Ir^{6f}-sites in the nanosheet, the higher activity of O^{cus} edge sides must be considered when describing am-hydr-IrO_x activity.

Our DFT calculations, which rely on the nanosheet atomistic model capturing the electronic and structural characteristics of am-hydr-IrO_x, propose new insights into the prospective active and inactive sites in am-hydr-IrO_x, revealing the likely species responsible for the higher activity of am-hydr-IrO_x compared to rutile-IrO_2 (Fig. S4, ESI†). Furthermore, our results substantiate the importance of modelling finite structures, morphologically analogous to the investigated am-hydr-IrO_x electrocatalyst and more closely mimicking real-world materials.

Discussion

Understanding the mechanisms underlying Ir dissolution and OER activity of an amorphous, highly dimensional iridium oxide catalyst, such as am-hydr-IrO_x, demands novel, applicable atomistic models beyond crystalline IrO_2 structures, capturing its high active surface area, unique hydroxylated Ir suboxide state, and multiple active sites. Our proposed nanosheet-based model aims to clarify factors limiting am-hydr-IrO_x performance, particularly its intrinsic trade-off between low stability against Ir dissolution and high OER activity. DFT-guided interpretations of experimental Ir L_3-edge XANES and EXAFS data, supported by the new nanosheet model, predicted the mechanisms behind the electronic and structural transformations of am-hydr-IrO_x across three potential regions (pre-redox, redox, and OER) with distinct thermodynamically driven transformations. Our dual-mechanistic nanosheet model offers a more comprehensive view, integrating chemical transformations (*e.g.*, deprotonation and OER intermediate formation) with spontaneous Ir dissolution both prior to and under

OER-relevant potentials, proposing parallel, complementary mechanisms operating in the redox and OER regions. This advances our understanding of the complex behaviour of am-hydr-IrO_x under OER conditions.

The nanosheet model's structural progression provides insights into am-hydr-IrO_x's comparatively inferior stability against Ir dissolution *versus* rutile-IrO_2.[4,11,33] Previous ICP-MS experiments on am-hydr-IrO_x reveal Ir dissolution beginning in the redox region, below 1.23 V_{RHE}, and peaking at $\sim$1.40 V_{RHE}.[4,11] In contrast to mechanistic explanations of kinetic-driven Ir dissolution *via* unstable solvated Ir^{3+} OER intermediate,[64] our study proposes a purely thermodynamically driven process of Ir loss, independent of OER mechanisms. Our theoretical model predicts Ir dissolution both below OER potentials in the redox region and the higher dissolution rates observed under OER potentials. Notably, the DFT-predicted potential ($\sim$1.35 V_{RHE}) for rapid formation of multiple adjacent Ir vacant sites (*i.e.*, a drastic loss of iridium atoms from the nanosheet atomistic model) aligns closely with the experimental maximum rate of Ir dissolution at $\sim$1.40 V_{RHE}.[4,11]

On the other hand, a few ordered layers of hydrous iridium oxides have shown higher stability against Ir dissolution,[42,70] likely related to their extended long-range ordering. Enhanced structural order would likely limit Ir defect site formation, *via* stabilizing surface terminations, however, further investigations of periodic systems using the presented theoretical model are required. Our atomistic model approach was also able to complement previous predictions about the thermodynamic instability of metal oxide couples under OER, which assumed the presence of OER pathways in the theoretical framework.[68,71]

The creation of new sites during the thermodynamically driven Ir defect formation process under OER potentials can prospectively trigger the participation of these new sites, beyond the inherent highly active edge sites. In fact, O-dangling bonds formed at these Ir defect sites are among the most active sites according to our calculations presented in Fig. 5. Since the O-dangling bonds, along with highly active edge sites, possess the shortest Ir–O bond lengths in the atomistic model, we propose that the degree of Ir–O bond contraction under OER potentials could be a good descriptor of the contribution of these highly active O-species, as captured by Fig. 4(d).

Though limited research has addressed the energetic behaviour and contribution to the OER activity of the Ir^{6f} metal sites, the nanosheet atomistic model presented in this study proposes their role to be significant in am-hydr-IrO_x and comparable to the active O-sites studied. In fact, nucleophilic H_2O attack is the bottleneck for the Ir^{6f} sites as well as for the defect-related O^{1f} sites and $*O^{cus}$–H edge sites in the nanosheet, consistent with previous studies on the rate-limiting nature of the H_2O attack on the electrophilic O^{I} species[8,29,72] (*i.e.*, edges and O^{1f} sites).

Generally, our results highlight the critical role of defect sites in the electrocatalytic activity of am-hydr-IrO_x. Thus, we suggest that hydrous iridium oxide-based electrocatalysts synthesized with high concentrations of pre-existing defect sites would yield a dense array of catalytically active sites, like O dangling bonds or edges. Recent literature reports promising approaches to tailor such materials, achieving a successful trade-off between OER activity and stability, such as core–shell IrO_x@$IrNiO_x$, where Ni leaching enhances defect density[65] or amorphous iridium (oxy) hydroxides where Li facilitates long-range order breaking.[73,74] Another strategy for long-term stabilization could involve beneficial interaction with the catalyst's support, *e.g.*, thin iridium oxide films on TiO_2 with core–shell morphology.[61]

Conclusions

This study introduces new key insights into the structural dynamics and electrocatalytic behaviour of am-hydr-IrO_x materials, alongside proposing a novel Ir dissolution mechanism. By examining a highly active and porous catalyst with a singular hydroxylated Ir suboxide species, comparing experimental *in situ* and *operando* Ir L_3-edge data with theory-predicted structures and surface terminations, we have developed a nanosheet atomistic model more representative of the physiochemical properties of am-hydr-IrO_x, surpassing conventional crystal-based models. DFT-supported analyses of experimentally observed electronic and structural changes reveal under redox potentials ($\sim$0.60–1.23 V_{RHE}) parallel deprotonation and spontaneous Ir loss *via* vacancy formation mechanisms, and under OER potentials ($>$1.23 V_{RHE}) rapid generation of multiple Ir defect sites, crucial for creating additional active sites despite the high cost of Ir loss, delving into previously unaddressed iridium dissolution mechanisms. Notably, the most active sites cluster around Ir defect sites and at edges, pointing to the importance of bulk defects in dictating electrocatalytic behaviour of am-hydr-IrO_x. Our results and approach challenge the traditional understanding of OER mechanisms in am-hydr-IrO_x and offer an alternative atomistic perspective, shedding light on the delicate relationship between OER activity and durability. In addition, we expect our findings to be broadly applicable to interpretations of the behaviour of other amorphous, hydrous iridium oxides, potentially guiding the development of more efficient and stable anode materials.

Experimental methods

Preparation of HIROF and electrochemical measurements

Electrochemical measurements were done in 0.5 M H_2SO_4, using a 1 × 1 cm Pt mesh (52 mesh woven, 0.1 mm diameter wire, 99.9% Alfa Aesar) as the counter electrode and a Mini HydroFlex reversible hydrogen electrode (Gaskatel) as the reference electrode (all potentials reported are relative to RHE) with a Biologic SP-300 potentiostat. HIROF synthesis involved continuous potential cycling of the Ir^0 substrate prepared by sputter deposition (see Supplementary Note 11 for preparation details, ESI†) between 0.05–1.5 V_{RHE} at 500 mV s^{-1} for a specified number of complete cycles (referred to as "HIROF$_n$" where 'n' indicates the number of cycles of growth), leading to the formation of highly porous am-hydr-IrO_x layer on top of the Ir^0 substrate. Cyclic voltammograms (CVs) from

0.05–1.5 V_{RHE} at 50 mV s^{-1} were conducted to assess the electrochemical behaviour of am-hydr-IrO_x in HIROF after different growth cycles (see Supplementary Note 1, ESI†). The OER activity of am-hydr-IrO_x in HIROF, was compared to the Ir^0 and rutile-IrO_2 references (see Supplementary Note 11 for preparation details, ESI†) using linear sweep voltammetry from 1.2 V_{RHE} to 1.6 V_{RHE} at a scan rate of 10 mV s^{-1} (see Supplementary Note 3, ESI†). Am-hydr-IrO_x possesses a higher activity (*i.e.*, higher current density at 1.6 V_{RHE}) than its anhydrous rutile-IrO_2 counterpart and the Ir^0 substrate from which it is grown.

Scanning electron microscopy (SEM)

Cross-section SEM images were obtained using a Hitachi S-1400 microscope operating at 5 kV. Thicknesses were measured using imageJ,[75] and the density estimation calculations are shown in Supplementary Note 2 (ESI†).

Cryogenic transmission electron microscopy (cryo-TEM)

Cryo-TEM imaging was performed using a JEOL JEM-2100 electron microscope (JEOL GmbH, Eching, Germany) operated at 200 keV. Deposition of am-hydr-IrO_x on TEM grids was performed by growing HIROF to 2000 cycles in 0.5 M H_2SO_4 and by ultra-sonication for 40 min, and a subsequent delamination of the am-hydr-IrO_x layer; a 4 μL drop was taken from the aqueous solution and drop-casted onto a lacey carbon-coated copper TEM grid (200 mesh, Electron Microscopy Sciences, Hatfield, PA). The TEM grid was then plunge-frozen in liquid ethane using a vitrobot (FEI Mark IV) set at 4 °C and 95% humidity. The TEM grid was transferred to the cryo-transfer holder of the microscope (Gatan 914, Gatan, Munich, Germany) and imaging was performed using a bottom-mounted 4*4k CMOS camera (TemCam-F416, TVIPS, Gauting, Germany). Imaging was carried out at temperatures around 93 K. For further information refer to Supplementary Note 12 (ESI†).

X-ray photoelectron spectroscopy (XPS)

In situ near-ambient pressure hard X-ray photoelectron spectroscopy (NAP-HAXPES) at 3 keV and 12 mbar was carried out at the SpAnTeX end-station[40] at the KMC-1 beamline[76] of BESSY II using a PHOIBOS 150 HV NAP electron analyser from SPECS. The electron analyser and the potentiostat (Biologic SP-300) shared a common grounding. Using the 'dip-and-pull' method with a 3-electrode configuration,[39–41] a thin film of electrolyte on the surface of the electrode was formed for the *in situ* growth of am-hydr-IrO_x, as shown in Fig. S6 in Supplementary Note 4 (ESI†). Thus, NAP-HAXPES measurements provided information of the hydrated condition of am-hydr-IrO_x.

The electronic structure of am-hydr-IrO_x in HIROF was measured by XPS conducted in ultra-high vacuum (UHV) with an Al K_α excitation X-ray source (1486.58 eV, PREVAC RS40B1) and a ScientaOmicron Argus CU analyzer in the energy materials *in situ* laboratory Berlin (EMIL).[77] The HIROF electrodes were rinsed with deionized water and dried in the Ar-filled glovebox antechamber (10^{-3} mbar) for ~2 hours prior to measurements (see Supplementary Note 5 for additional details, ESI†).

The *in situ* NAP-HAXPES and *ex situ* UHV Al K_α XPS Ir 4f spectra were fitted using the LMFIT python package[78] using an asymmetric finite Lorentzian[79] lineshapes for metallic Ir (Ir^0), rutile-IrO_2 (Ir^{4+}), and am-hydr-IrO_x, and a Shirley background. Further details on the fitting procedures and the complementary O 1s spectra can be found in the Supplementary Notes 4 and 5 (ESI†), respectively.

Ir L_3-edge X-ray absorption spectroscopy

The growth of HIROF to 1000 cycles and its response upon applied potentials (0.3–1.6 V_{RHE}) was studied by Ir L_3-edge X-ray absorption spectroscopy (XAS). Measurements were carried out at two different beamlines: KMC-3 at BESSY II, Germany[80,81] (Supplementary Note 13, ESI†) and NOTOS at ALBA, Spain (Supplementary Note 14, ESI†). Ir L_3-edge X-ray absorption near-edge structure (XANES) and extended X-ray absorption fine structure (EXAFS) measurements were collected to obtain simultaneous electronic and local geometric information. The *in situ* Ir L_3-edge XANES and EXAFS collected during HIROF growth presented in Fig. 1 were obtained at the KMC-3 beamline (raw XAS data and *in situ* electrochemical growth is shown in Supplementary Note 15 (ESI†), along with discussions of the correlation between WL position and WL intensity). The *in situ* Ir L_3-edge XANES and EXAFS of am-hydr-IrO_x under potential applications presented in Fig. 3 were collected at the NOTOS beamline (raw XAS data shown in Supplementary Note 16, ESI†). The experimental data collected from both beamlines exhibit strong correlations (Fig. S41 and S42 in Supplementary Note 17, ESI†), indicating a high level of agreement between the results obtained from different experimental setups. In addition, Fixed Energy X-ray Absorption Voltammetry (FEXRAV)[50] measurements at the KMC-3 beamline were also performed at the Ir^{4+} white-line energy with CVs recorded at 2 mV s^{-1} between 0.05 and 1.5 V_{RHE}.

For each XANES and EXAFS measurement, three spectra were collected and averaged. Some minor deglitching of small intensity spikes due to small bubbles and/or vibrations was removed using the Athena software,[82,83] a program in the IFEFFIT package. The signal-to-noise ratio of the oscillations was determined to be sufficient until k = 11 $Å^{-1}$, therefore EXAFS fittings were performed on k^2-weighted EXAFS spectra over a k-range of k = 3–11 $Å^{-1}$ (Fig. S38 in Supplementary Note 15, ESI†). Reasonable quantitative parameters could therefore be determined until R = ~4 Å for the first coordination shells of the Ir^0 and am-hydr-IrO_x components, which is sufficient for this work as it focusses on the short-range investigation of the local geometric structure of am-hydr-IrO_x.

The Ir L_3-edge XANES and EXAFS data were averaged and normalized using the Athena software.[82,83] For handling of the EXAFS data, the Larch software package[84] was used. The *ab initio* atomic scattering paths were constructed using the FEFF 8.0 code[85] within the Larch package.[84]

EXAFS fit analysis of the Ir^0 and rutile-IrO_2 references were used to determine the passive electron reduction factors (S_0^2) of the metallic and oxide iridium components used in the EXAFS fits of the *in situ* Ir L_3-edge EXAFS spectra of the HIROF system

(Supplementary Note 18, ESI†). Fittings of the *in situ* Ir L_3-edge EXAFS collected during HIROF growth to 1000 cycles were performed using a two-component structural model consisting of fcc-elemental Ir to model the Ir^0 substrate in HIROF, along with rutile-IrO_2 as an initial approximation for the am-hydr-IrO_x in HIROF (Supplementary Note 6, ESI†). A linear combination of the first coordination scattering paths was employed to determine the relative weight of the Ir^0 scattering path, which can be approximated to the nominal concentration of the Ir^0 within the sample environment. The EXAFS spectra were fitted over R = 1–3.5 Å using the first coordination shell scattering paths, with relaxed energy shift (ΔE_0) and Debye–Waller (σ) parameters, and constrained interatomic distances (R) and coordination numbers (CNs). The EXAFS fits are reported in Fig. S14 (ESI†) along with the fitting parameters in Table S3 in Supplementary Note 6 (ESI†). These EXAFS fittings were later repeated using the H-terminated nanosheet and stacked nanosheet structures (best fit structures), yielding the same mole fraction trend but with better r-factor fit values (Fig. S15 in Supplementary Note 6, ESI†).

Fittings of the *in situ* Ir L_3-edge EXAFS $HIROF_{1000}$ spectra were performed to obtain the atomic model that best describes am-hydr-IrO_x. Larch's scripting capabilities[84] enabled the efficient analysis of all structural options maintaining consistent input parameters, as opposed to the approach of using Artemis[82,83] which requires manual structure importing and fitting. This expedited the analysis and enabled tailored workflows to efficiently explore all structural options in the library provided by DFT. In these fittings, the parameters related to the Ir^0 substrate were fixed (*i.e.*, R, CN, and the mole fraction, 0.2 ± 0.1). All the oxygen scattering paths in the first coordination shell(s) of the library structures were included within the fit, and with their respective CN and R fixed, while only the ΔE_0 and σ parameters were allowed to vary within reason during the fitting process. Exclusion of structural options was made based on poor EXAFS fit parameters such as large r-factor values, large ΔE_0 shifts and negative σ values. See Supplementary Note 7 (ESI†) for further details.

Fittings of the *in situ* Ir L_3-edge EXAFS data of am-hydr-IrO_x after 1000 cycles of HIROF growth under potential application (Supplementary Note 16, ESI†) were focused on monitoring changes in the first coordination shell Ir–O bond length. A single component model, H-terminated nanosheet (Θ_H = 0.50 ML), was used to fit the region R = 1–2.1 Å, where the CN and R were also allowed to vary.

Density functional theory

All DFT calculations are performed using the projector augmented wave (PAW) method[86] as implemented in the VASP code.[87,88] The 5d and 6s states of Ir, and the 2s and 2p states of O are explicitly considered as the valence states. Electronic exchange and correlation (*xc*) are treated at the level of the semi-local generalized gradient approximation (GGA) functional due to Perdew–Burke–Ernzerhof (PBE)[89] and including the van der Waals (vdW) correction method of Tkatchenko and Scheffler (TS).[90] In addition, to estimate the contribution of an aqueous environment to the structures, energetics, and electronic structures of the iridium oxides, we apply an implicit solvation model in our surface calculations with a relative permittivity (ε_b) value of 80 to mimic the immediate water environment (Supplementary Note 20, ESI†). This is achieved *via* the VASPsol[91] subroutine, which is augmented to the VASP code. The kinetic energy cut-off of the planewave basis set is set to 700 eV for all calculations. The Brillouin zone integrations are carried out with reciprocal distances of $0.2/2\pi$ Å^{-1}, producing (12 × 12 × 8) k-grids with 131 irreducible k-points for bulk-layered IrO_2. Optimized lattice parameters for bulk-layered IrO_2 are determined by iteratively minimizing lattice stress and internal atomic displacements until the residual external pressure falls below 0.5 kbar. All 2D single-sheet structures are fully relaxed in the lateral directions with constraining the perpendicular lattice vector.

Supercell setup

All 2D nanosheet calculations are performed using periodic boundary condition supercell geometries, with a minimum vacuum separation of 15 Å. Symmetric layer models are employed within the sub-space of the $\begin{pmatrix} 4 & 0 \\ -2 & 4 \end{pmatrix}$ supercell, including 16 IrO_2 units. In order to obtain the most stable hydrogen adsorption configurations within this supercell setup, we calculate all symmetry inequivalent configurations for each hydrogen coverage without an implicit solvation model and select the most stable configurations for further calculations. Here, we note that ΔG can differ by up to 0.5 eV f.u.$^{-1}$ depending on configurations within the same hydrogen coverage (see Fig. S46, ESI†). Vacancies and surface reaction intermediates are calculated under assumption of OER *operando* conditions, all hydrogens at sheet surface are deprotonated consequently. We extend to explore this direction by considering edge sites. Similar to the procedure for the nanosheet surface, we initially identify the most stable edge termination under applied onset potentials. To achieve this, we employ a periodic supercell in which the edges of repeating ribbons representing the iridate nanosheets are separated by a 15 Å spacing. Each ribbon is 21 atomic rows wide to decouple its two edges, and a doubled periodicity along the sheet edge allows us to assess the stability of OER reaction intermediates at 0%, 50%, and 100% coverages. For comparison, we calculate rhombus-like (2·1) supercells of rutile (110) surfaces with various terminations. Periodic slabs are employed at the thickness of seven IrO_2 trilayers with a minimum vacuum separation of 20 Å.[61]

Ab initio thermodynamics

To determine the relative stabilities of possible nanosheet terminations, we employed the *ab initio* thermodynamics approach.[92,93] This yields the free energy change ΔG in comparison to the reference state of bulk layered IrO_2 as:

$$\Delta G = \frac{1}{n_{Ir}} G^{sys} - G^{bulk}_{IrO_2} - \left(\frac{n_O}{n_{Ir}} - 2\right) \cdot \mu_{H_2O} - \left\{\frac{n_H}{n_{Ir}} - 2 \cdot \left(\frac{n_O}{n_{Ir}} - 2\right)\right\} \cdot \left(\mu^{aq}_{H^+} + \mu_{e^-}\right), \quad (1)$$

where G^{sys}, $G^{bulk}_{IrO_2}$, μ_{H_2O}, $\mu^{aq}_{H^+}$ and μ_{e^-} represent the Gibbs free

energies of the nanosheet system and bulk layered IrO_2, as well as the chemical potentials of water, protons, and electrons, respectively. n_i (i = Ir, O, and H) is the number of each species in the periodic supercell used to describe the nanosheet system. To circumvent the computational description of $\mu^{aq}_{H^+}$, we adopted the computational hydrogen electrode (CHE) approach by Nørskov *et al.*[94] The CHE leverages the equivalence of $(\mu^{aq}_{H^+} + \mu_{e^-})$ to the chemical potential of hydrogen gas (μ_{H_2}) under standard conditions and the applied external potential U in relation to the reduced hydrogen electrode (RHE) at standard conditions under acidic environment.

$$\mu^{aq}_{H^+} + \mu_{e^-} = \frac{1}{2}\mu^{gas}_{H_2}(298.15\ \mathrm{K}, 1\ \mathrm{bar}) + eU, \tag{2}$$

As a result, we reformulated eqn (1) as,

$$\begin{aligned}\Delta G\ = &\frac{1}{n_{Ir}}G^{sys} - G^{bulk}_{IrO_2} - \left(\frac{n_O}{n_{Ir}} - 2\right)\cdot \mu_{H_2O} \\ &- \left\{\frac{n_H}{n_{Ir}} - 2\cdot\left(\frac{n_O}{n_{Ir}} - 2\right)\right\}\cdot\left(\frac{1}{2}\mu_{H_2} + eU\right),\end{aligned} \tag{3}$$

Here, following the approach of Reuter and Scheffler,[92] we approximated the Gibbs free energies G^{sys} and $G^{bulk}_{IrO_2}$ using zero-point energy (ZPE)-corrected total energies.[95] ZPE and entropic contributions to the chemical potentials of molecules (μ_{H_2O} and μ_{H_2}) were obtained from experimental reference tables.[96–98] Through the relationship between relative stabilities ΔG and applied potential U, relevant terminations at a certain U value can be determined in a phase diagram. The absolute value of the thermodynamic potentials derived from the CHE approach (*e.g.*, overpotential) should not be compared directly to experimentally measured values.

Author contributions

Marianne van der Merwe: conceptualization, methodology, investigation, data curation, formal analysis, visualization, writing – original draft. Yonghyuk Lee: methodology, investigation, data curation, formal analysis, visualization, writing – original draft. R. Enggar Wibowo: investigation, data curation, writing – review & editing. Tathiana Kokumai: investigation, data curation, formal analysis, writing – review & editing. Anna Efimenko: investigation, data curation, writing – review & editing. Mauricio Arce: investigation, data curation, writing – review & editing. Catalina E. Jimenez: investigation, data curation, writing – review & editing. Benjamin Howchen: investigation, data curation, writing – review & editing. Rosario Suarez Anzorena: investigation, data curation, writing – review & editing. Ilaria Lucentini: investigation, data curation, writing – review & editing. Carlos Escudero: investigation, data curation, writing – review & editing. Götz Schuck: investigation, data curation, writing – review & editing. Zdravko Kochovski: investigation, data curation, writing – review & editing. Marco Favaro: investigation, data curation, writing – review & editing. David E. Starr: investigation, data curation, writing – review & editing. Karsten Reuter: funding acquisition; resources, writing – review & editing. Christoph Scheurer: methodology, investigation, data curation, formal analysis, visualization, writing – original draft, resources, supervision. Marcus Bär: funding acquisition; resources, supervision, writing – review & editing. Raul Garcia-Diez: conceptualization, methodology, investigation, data curation, formal analysis, writing – original draft, project administration.

Conflicts of interest

There are no conflicts to declare.

Acknowledgements

This work was partially funded by the German Federal Ministry of Education and Research (BMBF) in the framework of the Kopernikus P2X project (ID: 03SFK2X0). Raul Garcia-Diez and Benjamin Howchen acknowledge support from BMBF in the framework of the project CatLab, Germany (03EW0015A/B). Marianne van der Merwe acknowledges the support from the Graduate School Materials for Solar Energy Conversion (MatSEC), as part of Dahlem Research School. The authors are grateful to the KMC-3 beamline at BESSY II (proposal: 221-10927), and the NOTOS beamline at ALBA (proposal: 2022097090) for providing access to beamtime for *in situ* Ir L_3-edge XAS measurements. The SpAnTeX end-station at the BESSY II synchrotron facility was financed by the Helmholtz Association through the Helmholtz Energy Materials Foundry (HEMF, GZ 714-48172-21/1). The authors thank Pip C. J. Clark and Michael J. Sear for their experimental assistance during the *in situ* NAP-HAXPES measurements at the SpAnTeX endstation, and Michael Haumann and Paul Beyer from FU Berlin for their assistance during the *in situ* Ir L_3-edge XAS measurements at KMC-3 beamline. The authors thank Alexander Steigert from the Institute of Nanospectroscopy, HZB for magnetron sputtering deposition of Ir^0 and IrO_2 thin films, and Carola Klimm from the Department Solution-Processing of Hybrid Materials and Devices, HZB for the SEM measurements. The Energy Materials *In Situ* Laboratory Berlin (EMIL) is acknowledged for providing the infrastructure for magnetron sputter thin film deposition, lab-source X-ray analytic measurements, and the use of the Chemistry Lab for electrochemical measurements. Open Access funding provided by the Max Planck Society.

References

1 R. Schlögl, *ChemSusChem*, 2010, **3**, 209–222.
2 M. Möckl, M. F. Ernst, M. Kornherr, F. Allebrod, M. Bernt, J. Byrknes, C. Eickes, C. Gebauer, A. Moskovtseva and H. A. Gasteiger, *J. Electrochem. Soc.*, 2022, **169**, 064505.
3 M. Bernt, C. Schramm, J. Schröter, C. Gebauer, J. Byrknes, C. Eickes and H. A. Gasteiger, *J. Electrochem. Soc.*, 2021, **168**, 084513.
4 O. Kasian, S. Geiger, T. Li, J. P. Grote, K. Schweinar, S. Zhang, C. Scheu, D. Raabe, S. Cherevko, B. Gault and K. J. J. Mayrhofer, *Energy Environ. Sci.*, 2019, **12**, 3548–3555.

5 M. Fathi Tovini, A. M. Damjanovic, H. A. El-Sayed, J. Speder, C. Eickes, J.-P. Suchsland, A. Ghielmi and H. A. Gasteiger, *J. Electrochem. Soc.*, 2021, **168**, 064521.
6 C. Massué, V. Pfeifer, M. van Gastel, J. Noack, G. Algara-Siller, S. Cap and R. Schlögl, *ChemSusChem*, 2017, **10**, 4786–4798.
7 V. A. Saveleva, L. Wang, D. Teschner, T. Jones, A. S. Gago, K. A. Friedrich, S. Zafeiratos, R. Schlögl and E. R. Savinova, *J. Phys. Chem. Lett.*, 2018, **9**, 3154–3160.
8 J. J. Velasco-Vélez, E. A. Carbonio, C.-H. Chuang, C.-J. Hsu, J.-F. Lee, R. Arrigo, M. Hävecker, R. Wang, M. Plodinec, F. R. Wang, A. Centeno, A. Zurutuza, L. J. Falling, R. V. Mom, S. Hofmann, R. Schlögl, A. Knop-Gericke and T. E. Jones, *J. Am. Chem. Soc.*, 2021, **143**, 12524–12534.
9 L. J. Frevel, R. Mom, J. J. Velasco-Vélez, M. Plodinec, A. Knop-Gericke, R. Schlögl and T. E. Jones, *J. Phys. Chem. C*, 2019, **123**, 9146–9152.
10 S. Cherevko, S. Geiger, O. Kasian, A. Mingers and K. J. J. Mayrhofer, *J. Electroanal. Chem.*, 2016, **773**, 69–78.
11 S. Cherevko, S. Geiger, O. Kasian, A. Mingers and K. J. J. Mayrhofer, *J. Electroanal. Chem.*, 2016, **774**, 102–110.
12 S. Cherevko, T. Reier, A. R. Zeradjanin, Z. Pawolek, P. Strasser and K. J. J. Mayrhofer, *Electrochem. Commun.*, 2014, **48**, 81–85.
13 S. Geiger, O. Kasian, M. Ledendecker, E. Pizzutilo, A. M. Mingers, W. T. Fu, O. Diaz-Morales, Z. Li, T. Oellers, L. Fruchter, A. Ludwig, K. J. J. Mayrhofer, M. T. M. Koper and S. Cherevko, *Nat. Catal.*, 2018, **1**, 508–515.
14 C. Liang, R. Rao, K. L. Svane, J. H. L. Hadden, B. Moss, S. Scott, M. Sachs, J. Murawski, A. M. Frandsen, D. J. Riley, M. P. Ryan, J. Rossmeisl, J. Durrant and I. E. L. Stephens, *Nat. Catal.*, 2024, **7**, 763–775.
15 S. B. Scott, J. E. Sørensen, R. R. Rao, C. Moon, J. Kibsgaard, Y. Shao-Horn and I. Chorkendorff, *Energy Environ. Sci.*, 2022, **15**, 1988–2001.
16 J. W. Zhao, K. Yue, H. Zhang, S. Y. Wei, J. Zhu, D. Wang, J. Chen, V. Y. Fominski and G. R. Li, *Nat. Commun.*, 2024, **14**, 2928.
17 M. Retuerto, L. Pascual, J. Torrero, M. A. Salam, Á. Tolosana-Moranchel, D. Gianolio, P. Ferrer, P. Kayser, V. Wilke, S. Stiber, V. Celorrio, M. Mokthar, D. G. Sanchez, A. S. Gago, K. A. Friedrich, M. A. Peña, J. A. Alonso and S. Rojas, *Nat. Commun.*, 2022, **13**, 7935.
18 E. Fabbri, A. Habereder, K. Waltar, R. Kötz and T. J. Schmidt, *Catal.: Sci. Technol.*, 2014, **4**, 3800–3821.
19 T. Reier, H. N. Nong, D. Teschner, R. Schlögl and P. Strasser, *Adv. Energy Mater.*, 2017, **7**, 1601275.
20 X. Rong, J. Parolin and A. M. Kolpak, *ACS Catal.*, 2016, **6**, 1153–1158.
21 A. Grimaud, A. Demortiere, M. Saubanere, W. Dachraoui, M. Duchamp, M. L. Doublet and J. M. Tarascon, *Nat. Energy*, 2017, **2**, 16189.
22 V. Pfeifer, T. E. Jones, J. J. Velasco Vélez, R. Arrigo, S. Piccinin, M. Hävecker, A. Knop-Gericke and R. Schlögl, *Chem. Sci.*, 2017, **8**, 2143–2149.
23 V. Pfeifer, T. E. Jones, S. Wrabetz, C. Massué, J. J. Velasco Vélez, R. Arrigo, M. Scherzer, S. Piccinin, M. Hävecker, A. Knop-Gericke and R. Schlögl, *Chem. Sci.*, 2016, **7**, 6791–6795.
24 O. Kasian, J. P. Grote, S. Geiger, S. Cherevko and K. J. J. Mayrhofer, *Angew. Chem., Int. Ed.*, 2018, **57**, 2488–2491.
25 K. Schweinar, B. Gault, I. Mouton and O. Kasian, *J. Phys. Chem. Lett.*, 2020, **11**, 5008–5014.
26 V. Pfeifer, T. E. Jones, J. J. Velasco Vélez, C. Massué, R. Arrigo, D. Teschner, F. Girgsdies, M. Scherzer, M. T. Greiner, J. Allan, M. Hashagen, G. Weinberg, S. Piccinin, M. Hävecker, A. Knop-Gericke and R. Schlögl, *Surf. Interface Anal.*, 2016, **48**, 261–273.
27 E. Willinger, C. Massué, R. Schlögl and M. G. Willinger, *J. Am. Chem. Soc.*, 2017, **139**, 12093–12101.
28 J. J. Velasco-Velez, L. J. Falling, D. Bernsmeier, M. J. Sear, P. C. J. Clark, T. S. Chan, E. Stotz, M. Hävecker, R. Kraehnert, A. Knop-Gericke, C. H. Chuang, D. E. Starr, M. Favaro and R. V. Mom, *J. Phys. D: Appl. Phys.*, 2021, **54**, 124003.
29 R. V. Mom, L. J. Falling, O. Kasian, G. Algara-Siller, D. Teschner, R. H. Crabtree, A. Knop-Gericke, K. J. J. Mayrhofer, J. J. Velasco-Vélez and T. E. Jones, *ACS Catal.*, 2022, **12**, 5174–5184.
30 J. J. Velasco Vélez, D. Bernsmeier, R. V. Mom, P. Zeller, Y. Shao-Horn, B. Roldan Cuenya, A. Knop-Gericke, R. Schlögl and T. E. Jones, *Adv. Energy Mater.*, 2024, 1–17.
31 P. G. Pickup and V. I. Birss, *J. Electroanal. Chem.*, 1987, **220**, 83–100.
32 L. D. Burke and E. J. O'Sullivan, *J. Electroanal. Chem.*, 1981, **117**, 155–160.
33 S. Geiger, O. Kasian, B. R. Shrestha, A. M. Mingers, K. J. J. Mayrhofer and S. Cherevko, *J. Electrochem. Soc.*, 2016, **163**, F3132–F3138.
34 V. Pfeifer, T. E. Jones, J. J. Velasco Vélez, C. Massué, M. T. Greiner, R. Arrigo, D. Teschner, F. Girgsdies, M. Scherzer, J. Allan, M. Hashagen, G. Weinberg, S. Piccinin, M. Hävecker, A. Knop-Gericke and R. Schlögl, *Phys. Chem. Chem. Phys.*, 2016, **18**, 2292–2296.
35 J. J. Velasco-Vélez, T. E. Jones, V. Streibel, M. Hävecker, C. H. Chuang, L. Frevel, M. Plodinec, A. Centeno, A. Zurutuza, R. Wang, R. Arrigo, R. Mom, S. Hofmann, R. Schlögl and A. Knop-Gericke, *Surf. Sci.*, 2019, **681**, 1–8.
36 L. D. Burke, N. S. Naser and B. M. Ahern, *J. Solid State Electrochem.*, 2007, **11**, 655–666.
37 L. Ouattara, S. Fierro, O. Frey, M. Koudelka and C. Comninellis, *J. Appl. Electrochem.*, 2009, **39**, 1361–1367.
38 S. Gottesfeld and S. Srinivasan, *J. Electroanal. Chem. Interfacial Electrochem.*, 1978, **86**, 89–104.
39 S. Axnanda, E. J. Crumlin, B. Mao, S. Rani, R. Chang, P. G. Karlsson, M. O. M. Edwards, M. Lundqvist, R. Moberg, P. Ross, Z. Hussain and Z. Liu, *Sci. Rep.*, 2015, **5**, 1–12.
40 M. Favaro, P. C. J. Clark, M. J. Sear, M. Johansson, S. Maehl, R. van de Krol and D. E. Starr, *Surf. Sci.*, 2021, **713**, 121903.
41 R. E. Wibowo, R. Garcia-Diez, T. Bystron, M. Prokop, M. van der Merwe, M. D. Arce, C. E. Jiménez, T.-E. Hsieh, J. Frisch, A. Steigert, M. Favaro, D. E. Starr, R. G. Wilks, K. Bouzek and M. Bär, *ACS Appl. Mater. Interfaces*, 2023, **15**, 51989–51999.
42 D. Weber, L. M. Schoop, D. Wurmbrand, S. Laha, F. Podjaski, V. Duppel, K. Müller, U. Starke and B. V. Lotsch, *J. Mater. Chem. A*, 2018, **6**, 21558–21566.

43 L. J. Frevel, R. Mom, J.-J. Velasco-Vélez, M. Plodinec, A. Knop-Gericke, R. Schlögl and T. E. Jones, *J. Phys. Chem. C*, 2019, **123**, 9146–9152.
44 S. Gottesfeld and S. Srinivasan, *J. Electroanal. Chem. Interfacial Electrochem.*, 1978, **86**, 89–104.
45 R. Kötz, *J. Electrochem. Soc.*, 1984, **131**, 72.
46 A. Zagalskaya and V. Alexandrov, *ACS Catal.*, 2020, **10**, 3650–3657.
47 A. Zagalskaya, I. Evazzade and V. Alexandrov, *ACS Energy Lett.*, 2021, **6**, 1124–1133.
48 B. E. Conway and J. Mozota, *Electrochim. Acta*, 1983, **28**, 9–16.
49 S. Laha, Y. Lee, F. Podjaski, D. Weber, V. Duppel, L. M. Schoop, F. Pielnhofer, C. Scheurer, K. Müller, U. Starke, K. Reuter and B. V. Lotsch, *Adv. Energy Mater.*, 2019, **9**, 1803795.
50 A. Minguzzi, O. Lugaresi, C. Locatelli, S. Rondinini, F. D'Acapito, E. Achilli and P. Ghigna, *Anal. Chem.*, 2013, **85**, 7009–7013.
51 V. I. Birss, C. Bock and H. Elzanowska, *Can. J. Chem.*, 1997, **75**, 1687–1693.
52 I. T. E. Fonseca, M. I. Lopes and M. T. C. Portela, *J. Electroanal. Chem.*, 1996, **415**, 89–96.
53 M. Hüppauff, *J. Electrochem. Soc.*, 1993, **140**, 598.
54 Y. Mo, I. C. Stefan, W. Bin Cai, J. Dong, P. Carey and D. A. Scherson, *J. Phys. Chem. B*, 2002, **106**, 3681–3686.
55 A. R. Hillman, M. A. Skopek and S. J. Gurman, *Phys. Chem. Chem. Phys.*, 2011, **13**, 5252–5263.
56 A. Minguzzi, O. Lugaresi, E. Achilli, C. Locatelli, A. Vertova, P. Ghigna and S. Rondinini, *Chem. Sci.*, 2014, **5**, 3591–3597.
57 A. Minguzzi, C. Locatelli, O. Lugaresi, E. Achilli, G. Cappelletti, M. Scavini, M. Coduri, P. Masala, B. Sacchi, A. Vertova, P. Ghigna and S. Rondinini, *ACS Catal.*, 2015, **5**, 5104–5115.
58 D. F. Abbott, D. Lebedev, K. Waltar, M. Povia, M. Nachtegaal, E. Fabbri, C. Copéret and T. J. Schmidt, *Chem. Mater.*, 2016, **28**, 6591–6604.
59 E. Oakton, D. Lebedev, M. Povia, D. F. Abbott, E. Fabbri, A. Fedorov, M. Nachtegaal, C. Copéret and T. J. Schmidt, *ACS Catal.*, 2017, **7**, 2346–2352.
60 D. Opalka, C. Scheurer and K. Reuter, *ACS Catal.*, 2019, **9**, 4944–4950.
61 Y. Lee, C. Scheurer and K. Reuter, *ChemSusChem*, 2022, **15**, 1–10.
62 L. D. Burke and D. P. Whelan, *J. Electroanal. Chem.*, 1981, **124**, 333–337.
63 L. D. Burke and D. P. Whelan, *J. Electroanal. Chem.*, 1984, **162**, 121–141.
64 O. Kasian, J. P. Grote, S. Geiger, S. Cherevko and K. J. J. Mayrhofer, *Angew. Chem., Int. Ed.*, 2018, **57**, 2488–2491.
65 H. N. Nong, T. Reier, H. S. Oh, M. Gliech, P. Paciok, T. H. T. Vu, D. Teschner, M. Heggen, V. Petkov, R. Schlögl, T. Jones and P. Strasser, *Nat. Catal.*, 2018, **1**, 841–851.
66 A. H. Reksten, A. E. Russell, P. W. Richardson, S. J. Thompson, K. Mathisen, F. Seland and S. Sunde, *Phys. Chem. Chem. Phys.*, 2020, **22**, 18868–18881.
67 J. Rossmeisl, Z. W. Qu, H. Zhu, G. J. Kroes and J. K. Nørskov, *J. Electroanal. Chem.*, 2007, **607**, 83–89.
68 T. Binninger, R. Mohamed, K. Waltar, E. Fabbri, P. Levecque, R. Kötz and T. J. Schmidt, *Sci. Rep.*, 2015, **5**, 1–7.
69 T. Naito, T. Shinagawa, T. Nishimoto and K. Takanabe, *Inorg. Chem. Front.*, 2021, **8**, 2900–2917.
70 Z. Liu, J. Qi, H. Zeng, Y. Zeng, J. Wang, L. Gu, E. Hong, M. Yang, Q. Fu, J. Chen and C. Yang, *ACS Appl. Energy Mater.*, 2022, **5**, 6869–6877.
71 T. Binninger, G. C. Moss, Z. S. H. S. Rajan, R. Mohamed and M. H. Eikerling, *ChemCatChem*, 2024, **16**(17), 202400567.
72 L. J. Falling, W. Jang, S. Laha, T. Götsch, M. W. Terban, S. Bette, R. Mom, J.-J. Velasco Vélez, F. Girgsdies, D. Teschner, A. Tarasov, C.-H. Chuang, T. Lunkenbein, A. Knop-Gericke, D. Weber, R. Dinnebier, B. V. Lotsch, R. Schlögl and T. E. Jones, *J. Am. Chem. Soc.*, 2024, **146**, 27886–27902.
73 J. Gao, C. Q. Xu, S. F. Hung, W. Liu, W. Cai, Z. Zeng, C. Jia, H. M. Chen, H. Xiao, J. Li, Y. Huang and B. Liu, *J. Am. Chem. Soc.*, 2019, **141**, 3014–3023.
74 J. Ruiz Esquius, D. J. Morgan, G. Algara Siller, D. Gianolio, M. Aramini, L. Lahn, O. Kasian, S. A. Kondrat, R. Schlögl, G. J. Hutchings, R. Arrigo and S. J. Freakley, *J. Am. Chem. Soc.*, 2023, **145**, 6398–6409.
75 C. A. Schneider, W. S. Rasband and K. W. Eliceiri, *Nat. Methods*, 2012, **9**, 671–675.
76 F. Schaefers, M. Mertin and M. Gorgoi, *Rev. Sci. Instrum.*, 2007, **78**, 123102.
77 S. Hendel, F. Schäfers, M. Hävecker, G. Reichardt, M. Scheer, J. Bahrdt and K. Lips, *AIP Conf. Proc.*, 2016, **1741**, 030038.
78 M. Newville, T. Stensitzki, D. B. Allen, M. Rawlik, A. Ingargiola and A. Nelson, *Astrophysics Source Code Library*, 2016, DOI: 10.5281/zenodo.11813.
79 G. H. Major, D. Shah, V. Fernandez, N. Fairley and M. R. Linford, *Vac. Tech. Coat.*, 2020, 35–40.
80 G. Schuck and I. Zisak, *J. Large-Scale Res. Facilities*, 2020, **6**, 139.
81 I. Zizak and P. Gaal, *J. Large-Scale Res. Facilities*, 2017, **3**, A123.
82 B. Ravel and M. Newville, *J. Synchrotron Radiat.*, 1995, **12**, 537–541.
83 B. Ravel and M. Newville, *Phys. Scr.*, 2005, 1007–1010.
84 M. Newville, *J. Phys.: Conf. Ser.*, 2013, **430**, 012007.
85 A. L. Ankudinov, B. Ravel, J. J. Rehr and S. D. Conradson, *Phys. Rev. B: Condens. Matter Mater. Phys.*, 1998, **58**, 7565–7576.
86 G. Kresse and D. Joubert, *Phys. Rev. B: Condens. Matter Mater. Phys.*, 1999, **59**, 1758–1775.
87 G. Kresse and J. Hafner, *Phys. Rev. B: Condens. Matter Mater. Phys.*, 1993, **47**, 558–561.
88 G. Kresse and J. Furthmüller, *Phys. Rev. B: Condens. Matter Mater. Phys.*, 1996, **54**, 11169–11186.
89 J. P. Perdew, K. Burke and M. Ernzerhof, *Phys. Rev. Lett.*, 1996, **77**, 3865–3868.
90 A. Tkatchenko and M. Scheffler, *Phys. Rev. Lett.*, 2009, **102**, 073005.
91 K. Mathew, R. Sundararaman, K. Letchworth-Weaver, T. A. Arias and R. G. Hennig, *J. Chem. Phys.*, 2014, **140**(8), DOI: 10.1063/1.4865107.
92 K. Reuter and M. Scheffler, *Phys. Rev. B: Condens. Matter Mater. Phys.*, 2001, **65**, 035406.

93 K. Reuter, *Catal. Lett.*, 2016, **146**, 541–563.
94 J. K. Nørskov, J. Rossmeisl, A. Logadottir, L. Lindqvist, J. R. Kitchin, T. Bligaard and H. Jónsson, *J. Phys. Chem. B*, 2004, **108**, 17886–17892.
95 Q. Sun, K. Reuter and M. Scheffler, *Phys. Rev. B: Condens. Matter Mater. Phys.*, 2003, **67**, 205424.
96 W. S. Benedict, N. Gailar and E. K. Plyler, *J. Chem. Phys.*, 1956, **24**, 1139–1165.
97 K. K. Irikura, *J. Phys. Chem. Ref. Data*, 2007, **36**, 389–397.
98 M. W. Chase, J. L. Curnutt, J. R. Downey, R. A. McDonald, A. N. Syverud and E. A. Valenzuela, *J. Phys. Chem. Ref. Data*, 1974, **11**, 311–480.